

FINITE ELEMENT ANALYSIS OF THREE-DIMENSIONAL ELASTO-PLASTIC SINUSOIDAL
CONTACT AND INCLUSION IN A MULTI-SCALE ROUGH SURFACE CONTACT MODEL

Except where reference is made to the work of others, the work described in this thesis is my own or was done in collaboration with my advisory committee. This thesis does not include proprietary or classified information.

Vijaykumar Krithivasan

Certificate of Approval:

Pradeep Lall
Thomas Walter Professor
Mechanical Engineering

Robert L. Jackson, Chair
Assistant Professor
Mechanical Engineering

Hareesh V. Tippur
Alumni Professor
Mechanical Engineering

George T. Flowers
Interim Dean, Graduate School

FINITE ELEMENT ANALYSIS OF THREE-DIMENSIONAL ELASTO-PLASTIC SINUSOIDAL
CONTACT AND INCLUSION IN A MULTI-SCALE ROUGH SURFACE CONTACT MODEL

Vijaykumar Krithivasan

A Thesis

Submitted to

the Graduate Faculty of

Auburn University

in Partial Fulfillment of the

Requirements for the

Degree of

Master of Science

Auburn, Alabama
May 10, 2008

FINITE ELEMENT ANALYSIS OF THREE-DIMENSIONAL ELASTO-PLASTIC SINUSOIDAL
CONTACT AND INCLUSION IN A MULTI-SCALE ROUGH SURFACE CONTACT MODEL

Vijaykumar Krithivasan

Permission is granted to Auburn University to make copies of this thesis at its
discretion, upon the request of individuals or institutions and at
their expense. The author reserves all publication rights.

Signature of Author

Date of Graduation

VITA

Vijaykumar Krithivasan, son of Mr. B. Krithivasan and K. Sathyabama was born in Bangalore, India on March 26, 1981. He graduated high school from Sri Sankara Senior Secondary School, Chennai in April 1999. He graduated from University of Madras, Madras, India with a Bachelor of Engineering degree in July 2003. He began his graduate studies in Mechanical Engineering at Auburn University in January 2005.

THESIS ABSTRACT

FINITE ELEMENT ANALYSIS OF THREE-DIMENSIONAL ELASTO-PLASTIC SINUSOIDAL
CONTACT AND INCLUSION IN A MULTI-SCALE ROUGH SURFACE CONTACT MODEL

Vijaykumar Krithivasan

Master of Science, May 10, 2008
(B.E., University of Madras, 2003)

104 Typed Pages

Directed by Robert L. Jackson

Researchers have developed many models to simulate the elasto-plastic contact of spheres. However, there does not appear to exist a closed-form analytical model for elasto-plastic three dimensional sinusoidal contact. This work uses a finite element model (FEM) to characterize elasto-plastic sinusoidal contact. Although at initial contact the spherical and sinusoidal cases are very similar and can both be described by the classic elastic Hertz contact case, once the contact is pressed past a certain range of inelastic deformation the two cases are very different. The FEM model is used to produce equations which can be employed to approximately relate the area of contact to the contact pressure for elasto-plastic sinusoidal contact. The equations are obtained by fitting to the FEM results and existing elastic solutions to sinusoidal contact. An empirical expression for the average pressure which causes complete contact between elasto-plastic sinusoidal contacts was also developed. The results showed that the required pressure for complete contact is significantly less in the elasto-plastic regime than the elastic regime. In addition, this pressure is shown to be greater than the traditional hardness, of $3 \cdot S_y$.

One of the major motivations for this work was to generate a model that could be used in sinusoidal and frequency based rough surface contact models. A multiscale model is a non-statistical model and non-fractal that is used to describe normal contact between rough surfaces featuring multiple scales. The empirical equations developed in the sinusoidal contact model are used to characterize asperity contact in the multiscale contact model. Based on this, predictions are made for contact area as a function of applied load. It was interesting to note that the real area of contact versus the applied load exhibits a linear relationship for both elastic and elasto-plastic cases up until the surface is completely flattened out. As expected, the real area of contact undergoing elasto-plastic deformation predicted by the multiscale model was higher than when the surface is undergoing elastic deformation. For a given applied load it was also found that the lower frequency ranges, as opposed to higher frequency ranges, dictated the predicted level of real contact area.

ACKNOWLEDGMENTS

I am deeply indebted to Dr. Robert.L.Jackson for his technical, educational, and moral support throughout my master's program. I am deeply influenced by his research and teaching philosophy which made my graduate work an educational and professionally enriching experience. I am grateful to Dr. Hareesh.V.Tippur for providing a great deal of encouragement and technical support. I would also like to thank Dr. Pradeep Lall for his encouragement and for agreeing to be on my master's thesis committee.

I would like to thank my colleagues Mr. Everett Wilson, Mr. Jeremy Dawkins and Mr. Santosh Angadi at the Multiscale Tribology Laboratory here at Auburn university.

I am grateful to my friends Ms. Anjeli Singh, Dr. Vivek Krishnan, Mr. Kashyap Yellai, Mr. Anand Sankarraaj, Mr. Karthik Narayanan, Ms. Kavita Arumugam, Mr. Sankar Balasubramanian, Mr. Raghu Viswanathan, Mr. Naren Parinar, Ms. Rebecca Ibrahim, and Mr. Sumit Sen for their support and encouragement.

Finally, I would like to thank my family for their unwavering support and encouragement throughout my master's program. Many sacrifices made by my parents Krithivasan and Satyabama cannot be described in words. My brother, Dr. Ramkumar Krithivasan, has been a pillar of support throughout my life. His achievements have always been a motivation for me to move forward. I am forever indebted to my family.

Style manual or journal used LATEX: A Document Preparation System by Leslie Lamport (together with the style known as “aums”) and Bibliography as per Tribology Transactions

Computer software used TEX (specifically LATEX), VossPlot, ANSYS, MATLAB 7.0.4, MS Office Excel 2003 and the departmental style-file aums.sty

TABLE OF CONTENTS

LIST OF FIGURES	xi
LIST OF TABLES	xiii
NOMENCLATURE	xiv
1 INTRODUCTION	1
1.1 Organization of thesis	2
2 LITERATURE REVIEW	3
2.1 Introduction	3
2.2 Spherical contact models	5
2.3 Elastic sinusoidal contact	10
2.4 Elasto-plastic sinusoidal contact	11
2.5 Statistical contact model	16
2.6 Fractal contact model	17
3 FINITE ELEMENT MODEL	20
3.1 Introduction	20
3.2 Building the solid model	20
3.3 Mesh convergence test	21
3.4 Simulation methodology	23
3.5 Verification of model accuracy	27
4 ELASTO-PLASTIC FEM RESULTS	29
4.1 Introduction	29
4.2 Parametric study	29
4.3 Critical elasto-plastic pressure estimation	34
4.4 Real contact area estimation	42
4.5 The empirical model	45
5 MULTISCALE ROUGH SURFACE CONTACT MODEL	50
5.1 Introduction	50
5.2 Multiscale model foundation	50
5.3 Elasto-plastic multiscale model	54
5.4 Frequency spectrum for different surfaces	54
5.5 Frequency level iteration versus contact area	58
5.6 Elasto-plastic and elastic comparison	62

6	CONCLUSIONS	67
	BIBLIOGRAPHY	69
	APPENDICES	72
A	DERIVATION OF CRITICAL VALUES FOR SINUSOIDAL CONTACT	73
B	MATLAB CODE FOR CONTACT AREA VERSUS FREQUENCY ITERATION	76
C	MATLAB CODE FOR FREQUENCY SPECTRUM AND LOAD VERSUS CONTACT AREA	84

LIST OF FIGURES

2.1	Topographical contour plot of the sinusoidal surface geometry.	4
2.2	Cross-section of sinusoidal type contact.	6
2.3	Diagram of the hypothetical progression of change in hardness with geometry for spherical and sinusoidal contact.	13
2.4	Compressed cavity of material.	14
2.5	Islands defined by a horizontal section.	18
3.1	Uniform mesh on the rigid flat formed by 21x21 array of elements.	22
3.2	Schematic of degree of freedom restraints used for the one quarter sinusoidal FEM model (actual modeled geometry is much longer in the z direction).	24
3.3	Various stages of contact.	25
3.4	Deformation history.	26
3.5	Comparison of elastic FEM results with JGH model.	28
4.1	$\frac{p}{S_y}$ versus contact area ratio ($A \cdot F^2$) for different yield strength.	31
4.2	Contact area ratio ($A \cdot F^2$) versus \bar{p}/p^* for different yield strength.	32
4.3	The effect of S_y/E' on pressure to cause complete contact.	35
4.4	The effect of Δ/λ on pressure to cause complete contact.	37
4.5	Contact area ratio ($A \cdot f^2$) versus \bar{p}/p_{ep}^* for different yield strength values.	39
4.6	Contact area ratio ($A \cdot f^2$) versus \bar{p}/p_{ep}^* for different values of Young's Modulus E.	40
4.7	Contact area ratio ($A \cdot f^2$) versus \bar{p}/p_{ep}^* for different values of the dimensionless geometric quantity Δ/λ	41

4.8	Comparison of the FEM results and the elasto-plastic sinusoidal contact model (marked by lines) given by Eq. 4.8 for different yield strength values.	46
4.9	Comparison of the FEM results and the elasto-plastic sinusoidal contact model (marked by lines) given by Eq. 4.8 for different Young's modulus values.	48
4.10	Comparison of the FEM results and the elasto-plastic sinusoidal contact model (marked by lines) given by Eq. 4.8 for different sinusoidal geometries.	49
5.1	Flow chart of iterative asperity contact model.	53
5.2	Frequency spectrum of surface 1.	55
5.3	Frequency spectrum of surface 2.	56
5.4	Frequency spectrum of surface 3.	57
5.5	Contact area ratio versus frequency iteration for surface 1.	59
5.6	Contact area ratio versus frequency iteration for surface 2.	60
5.7	Contact area ratio versus frequency iteration for surface 3.	61
5.8	Elastic and Elasto-Plastic contact area versus applied load for surface 1. . .	64
5.9	Elastic and Elasto-Plastic contact area versus applied load for surface 2. . .	65
5.10	Elastic and Elasto-Plastic contact area versus applied load for surface 3. . .	66

LIST OF TABLES

3.1	Material properties	27
4.1	Parametric study based on the Yield Strength S_y	30
4.2	Parametric study based on the Young's Modulus E'	33
4.3	Parametric study based on the Geometric ratio Δ/λ	33
4.4	Variation of $\frac{p_{ep}^*}{p^*}$ (FEM) and $\frac{p_{ep}^*}{p^*}$ (Fit Eq. 4.1) with respect to S_y/E'	36
4.5	Variation of $\frac{p_{ep}^*}{p^*}$ (FEM) and $\frac{p_{ep}^*}{p^*}$ (Fit Eq. 4.1) with respect to Δ/λ	38

NOMENCLATURE

\bar{A}	individual asperity contact area
\bar{A}_i	single asperity contact area
\bar{F}_i	single asperity contact load
\bar{P}	contact load
\bar{p}	average pressure over entire surface
β_i	amplitude at the i^{th} level
η_i	areal asperity density at the i^{th} level
γ	scaling parameter
λ	wavelength ($\frac{1}{f}$)
ω_c	critical interference between hemisphere and surface
ω	interference between hemisphere and surface
$\phi(z)$	gaussian distribution
$\phi_{m,n}$	random phase
$\sigma_{lateral}$	lateral stress
σ	standard deviation of surface heights
τ_y	Shear strength

Δ	amplitude of sinusoidal surface
ν	Poisson's ratio
A_c	critical area of contact value at onset of plastic deformation
A_E	area of contact
A_{JGH}	area of contact from model by Johnson et al. [1]
A_{KE}	area of contact from model by Kogut and Etsion [2]
A_r	real area of contact
C_s	non-dimensional load constant
D	fractal dimension $2 < D < 3$
E	elastic modulus
E'	reduced elastic modulus
F	contact load
f	spatial frequency (reciprocal of wavelength)
F_μ	Friction force
F_E	contact force
f_i	reciprocal of wavelength at the i^{th} level
G	fractal roughness
h	height of sinusoidal surface from base

L	sample length
M	number of superimposed ridges
n	frequency index
n_{max}	upper limit of n
p	average contact pressure
p^*	average pressure for complete contact
p_{ep}^*	critical pressure for elasto-plastic complete contact
R	radius of curvature of tip of sinusoidal surface or hemispherical asperity
z	height of asperity density measured from the mean of asperity heights
S_y	yield strength

CHAPTER 1

INTRODUCTION

Computational modeling of contact between surfaces, or contact mechanics, has been realized as an important field for many years, probably starting sometime around the classic solution of elastic spherical contact developed by Hertz in 1888 (originally developed to model optical contacts) [3]. Since then the field has evolved to consider rough surface contact between mechanical devices and more recently in MEMS. Many earlier models [4]–[10] employed mostly spherical contact models to simulate individual asperity peaks on a surface. Several used alternative approaches to model periodic surface roughness as sine waves [1, 11]. These first models considered only elastic contact. However, due to the high loads often seen in contact situations, the stresses can cause plastic deformation as well. The FFT based contact methodology outlined by Stanley and Kato [12] made use of these elastic contact models to model rough surface contact by first transforming the surface data into the frequency domain.

In keeping with the need for a new deformation model which could be easily incorporated into the frequency based rough surface contact models, the current work develops an elasto-plastic sinusoidal contact model. Empirical equations were developed that fully characterize a sinusoidal surface undergoing elasto-plastic deformation. The developed equations were used inside the multiscale model foundation to predict the real area of contact as a function of applied load. Since the multiscale model uses Fourier series, and it consists series of sine waves, it would be logical to model the asperities as an array of stacked sine waves.

Therefore sinusoidal contact model should be used instead of spherical contact models in the multiscale model.

1.1 Organization of thesis

Chapter 2 of this thesis presents a thorough background on different types of contact models ranging from spherical type contact to sinusoidal type contact.

Chapter 3 (also published in [13]) presents the modeling methodology employed in formulating the Finite Element Model (FEM). This chapter is divided into three sections. The first section of this chapter describes how the solid model is built for the finite element analysis. The second section deals with the mesh convergence that was achieved. The third section titled *Simulation methodology* deals with how the finite element method employed the displacement method for the analysis.

Chapter 4 (also published in [13]) is divided into four sections. The first describes in detail the elasto-plastic FEM results obtained from the model. The remaining sections present the various mathematical fits that were generated in estimation of real contact area and average contact pressure.

In Chapter 5 the multi-scale model for elasto-plastic contact of rough surfaces is presented. Here the mathematical fit is incorporated into the multi-scale model.

Chapter 6 concludes the thesis with a summary of the finite element analysis results.

CHAPTER 2

LITERATURE REVIEW

2.1 Introduction

Elasto-plastic sinusoidal contact has recently become more important with the development of several multiscale rough surface contact models [14]–[20]. This is because some of these multiscale rough surface contact models use a Fourier series to consider the different scales. Since a Fourier series consists of a series of sine waves with different amplitudes and periods, it is logical to use sinusoidal contact models to consider individual asperity contact. Sinusoidal contact in some cases may be a more realistic depiction of surface contact than spherical contact. Intuitively, surface asperities should overall be shaped more like sine waves than hemispheres. A model of elasto-plastic sinusoidal contact would be very useful to these multiscale contact models. Gao et al. [21] modeled two-dimensional sinusoidal contact using the finite element method, and made note of some interesting results which will also be considered in the current analysis. Gao et al. [21] reported a $H/S_y = 5.8$ for the elasto-plastic case. The current work finds trends similar to [21] resulting from the three-dimensional elastic case. It was interesting to note that the H/S_y for the 3D elasto-plastic case was not restricted to 5.8 as reported by Gao et al. [21].

This chapter elucidates various rough surface contact models such as the statistical contact model, the fractal contact model and the multiscale contact model. A justification for inclusion of sinusoidal deformation model into the multiscale model foundation is also provided.

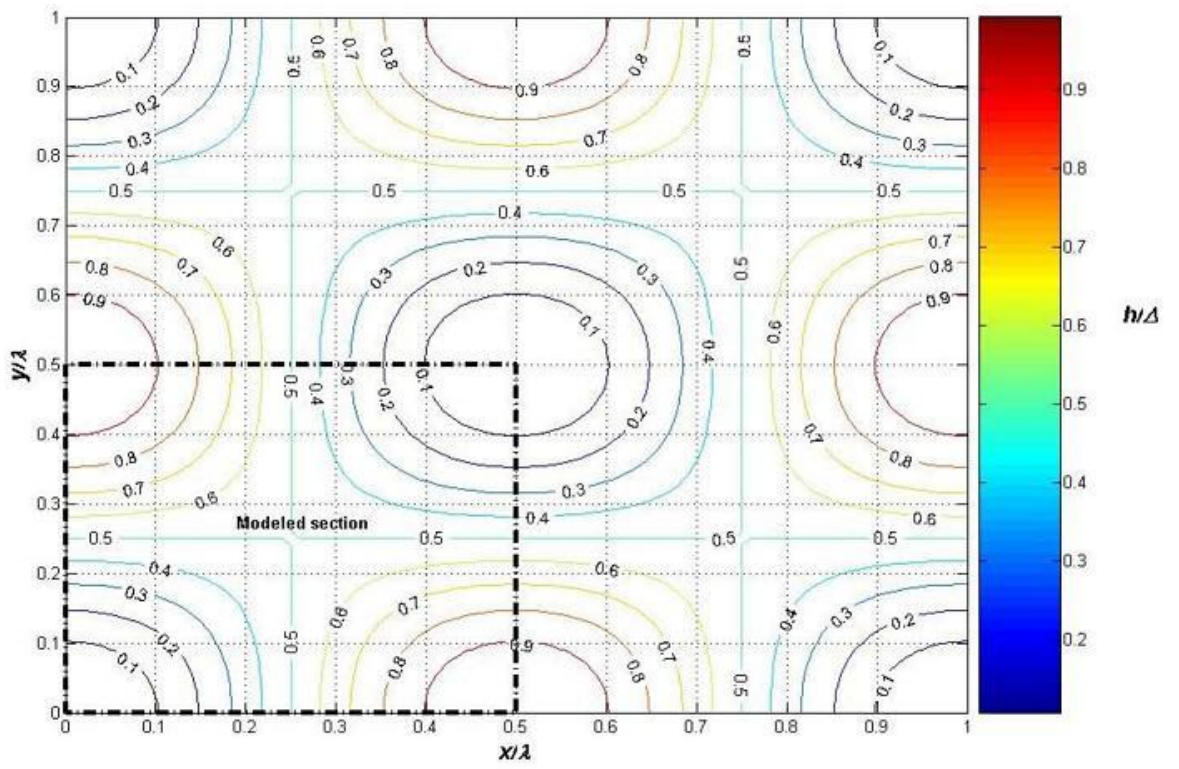


Figure 2.1: Topographical contour plot of the sinusoidal surface geometry.

2.2 Spherical contact models

Although the following section may at first seem off subject, in reality spherical contact is very useful for modeling sinusoidal contact, especially when the deformation is restricted to the tips of the peaks (see Fig. 2.2). For this reason, Johnson et al. [1] provides two limiting solutions to three dimensional sinusoidal contact, and the first being based upon the Hertz elastic spherical contact solution. The Hertz solution provides closed-form expressions to the deformations and stresses of two spheres in a purely elastic contact. The two spheres may have different radii and different elastic properties. However, the closed-form solutions render an equivalent case where a single elastic sphere, having an equivalent elastic modulus, E' , and an equivalent radius, R , is in contact with a rigid flat (see Eqs. 2.1– 2.4 that follow).

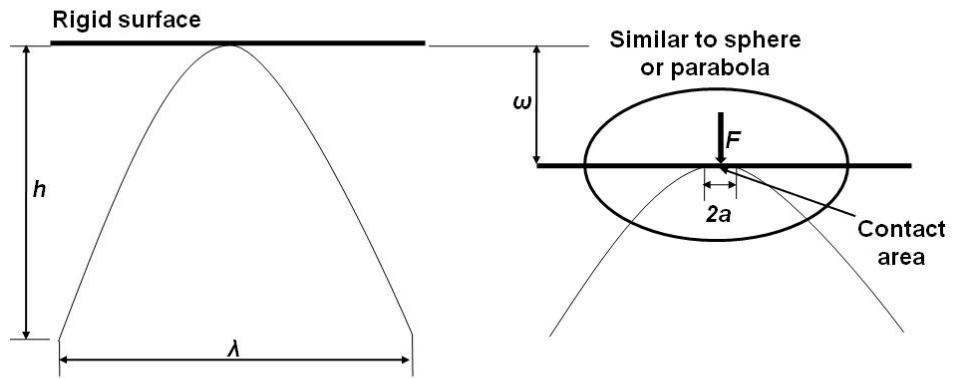


Figure 2.2: Cross-section of sinusoidal type contact.

The interference, ω , can be described as the distance the sphere is displaced normally into the rigid flat. The Hertz solution assumes that the interference is small enough such that the geometry does not change significantly. The solution also approximates the sphere surface as a parabolic curve with an equivalent radius of curvature at its tip. The resulting equations for contact radius and load from the Hertz solution are:

$$A_E = \pi R \omega \quad (2.1)$$

$$F_E = \frac{4}{3} E' \sqrt{R} (\omega)^{\frac{3}{2}} \quad (2.2)$$

where

$$\frac{1}{E'} = \frac{1 - \nu_1^2}{E_1} + \frac{1 - \nu_2^2}{E_2} \quad (2.3)$$

$$\frac{1}{R'} = \frac{1}{R_1} + \frac{1}{R_2} \quad (2.4)$$

and $E_1, \nu_1, R_1, E_2, \nu_2, R_2$, are the elastic properties and radii of sphere 1 and 2, respectively.

Again, since the sinusoidal surface and the tip of a sphere are very similar at initial contact, the initiation of plastic deformation (defined as the critical interference) can be derived from Hertz contact theory, but can also be used for sinusoidal contact for cases of relatively small loads and interferences. The critical values of interference, area, and load

are derived for the case of initial sinusoidal contact (when the contact geometry is still similar to a parabola or sphere) in Appendix A.

Kogut and Etsion [2] performed a finite element analysis of the case of an elastic-perfectly plastic sphere in contact with a rigid flat. Their work gives a very detailed analysis of the stress distribution in the contact region, and piecewise empirical expressions are provided for the contact area, the contact force, and the average contact pressure. At values $\omega/\omega_c < 1$ the Hertz contact solution is assumed. Two sets of equations are provided for the ranges $1 < \omega/\omega_c < 6$, and $6 < \omega/\omega_c < 110$. They describe the deformation only up to $\omega/\omega_c = 110$, at which point full plasticity is assumed. In their analysis, the value of hardness, H , is set to be fixed at $2.8 \cdot S_y$. Jackson and Green [22] also provide a more complicated model which may describe large deformations better than the Kogut and Etsion (KE) model. The most notable difference being that H is often much less than $2.8 \cdot S_y$ for high loads. However, Quicksall et al. [23] found that the Jackson and Green and KE model agree fairly well for small deformations and the KE model is also much easier to algebraically manipulate. For these reasons, the KE model is used in the current work to model the initial elasto-plastic deformation of the sinusoidal surfaces.

The KE model is used in the current work to obtain an empirical relationship between contact pressure and area. Since the current work is mostly concerned with spherical contact for small load and interferences, the pressure-interference and the area-interference relation's for $1 < \omega/\omega_c < 6$ from Kogut and Etsion [2] are used:

$$\left(\frac{p}{S_y} \right) = 1.19 \left(\frac{\omega}{\omega_c} \right)^{0.289} \quad (2.5)$$

$$\left(\frac{A_{KE}}{A_c} \right) = 0.93 \left(\frac{\omega}{\omega_c} \right)^{1.136} \quad (2.6)$$

With some manipulation Eq. 2.5 becomes

$$\frac{\omega}{\omega_c} = \left[\frac{1}{1.19} \left(\frac{p}{S_y} \right) \right]^{\frac{1}{0.289}} \quad (2.7)$$

The average contact pressure, p , is related to the average pressure, \bar{p} , over the sinusoidal surface by:

$$p = \left(\frac{\bar{p}}{2 \cdot A_{KE}} \lambda^2 \right) \quad (2.8)$$

The \bar{p} denotes average pressure over the entire surface, including areas that are not in contact while p denotes average contact pressure, just in the contact area. When complete contact occurs, $\bar{p} = p$. Substituting Eq. 2.7 and 2.8 into Eq. 2.6 the following is obtained:

$$\frac{A_{KE}}{A_c} = \left(\frac{\bar{p}}{2 \cdot A_{KE} \cdot S_y \cdot 1.19} \lambda^2 \right)^{3.93} \quad (2.9)$$

Further solving for A_{KE} results in the equation below:

$$A_{KE} = (A_c)^{\frac{1}{4.93}} \left(\frac{\bar{p}}{2.38 \cdot S_y} \lambda^2 \right)^{\frac{3.93}{4.93}} \quad (2.10)$$

An equation similar to Eq. 2.10 is used in the current work to model initial elasto-plastic contact of the sinusoidal surfaces. This is explained in more detail later.

2.3 Elastic sinusoidal contact

The analysis for the case of 3-D waviness developed by authors Johnson, Greenwood and Higginson [1] (hereafter referred to as "JGH") provides a relation between pressure and contact area. First \bar{p} is defined as the average pressure on the surface (considering both contacting and non-contacting regions) and p^* is the amplitude of a sinusoidal pressure superimposed on the mean pressure that yields complete contact. Complete contact is defined as when the entire sinusoidal surface is flattened and in contact with the opposing surface (i.e. there is no gap between the surfaces). The amplitude of the pressure profile, p^* is given as:

$$p^* = \sqrt{2\pi} E' \Delta f \quad (2.11)$$

where E' is the reduced elastic modulus, Δ is the amplitude of the sinusoidal surface, and f is the frequency or reciprocal of wavelength, λ . Thus when $\bar{p} \geq p^*$, the pressure loads the surfaces so that there is no gap between them. Alternatively, when $\bar{p} < p^*$ the contact is not complete, and a closed form solution for the three-dimensional waviness contact problem is not available. However, Johnson et al. [1] provides two asymptotic solutions to the problem. For $\bar{p} \ll p^*$ the following equation derived from Hertz contact theory applies:

$$(A_{JGH})_1 = \frac{2\pi}{f^2} \left[\frac{3}{8\pi} \frac{\bar{p}}{p^*} \right]^{\frac{2}{3}} \quad (2.12)$$

and when \bar{p} approaches p^* (i.e., contact is nearly complete) the following equation applies:

$$(A_{JGH})_2 = \frac{1}{f^2} \left(1 - \frac{3}{2\pi} \left[1 - \frac{\bar{p}}{p^*} \right] \right) \quad (2.13)$$

Since no general analytical solution is available, an equation linking Eqs. 2.12 and 2.13 is fit by Jackson and Streater [14] to the experimental and numerical data provided by Johnson et al. [1]:

For $\frac{\bar{p}}{p^*} < 0.8$:

$$A = (A_{JGH})_1 \left(1 - \left[\frac{\bar{p}}{p^*} \right]^{1.51} \right) + (A_{JGH})_2 \left(\frac{\bar{p}}{p^*} \right)^{1.04} \quad (2.14)$$

For $\frac{\bar{p}}{p^*} \geq 0.8$:

$$A = (A_{JGH})_2 \quad (2.15)$$

2.4 Elasto-plastic sinusoidal contact

The previous cases of elasto-plastic spherical contact and elastic sinusoidal contact are now sufficiently expanded using finite element results so that a model of elasto-plastic sinusoidal contact can be formulated. Since it has been established that at low deformations the sinusoidal contact will behave similarly to the spherical contact, this work will focus mostly on the case of heavy deformations in sinusoidal contact.

Intuitively, the hardness of a sinusoidal shaped contact will follow a much different trend than the spherical case. As shown in the Fig. 2.4, the slope of the surface at the edge of contact for the sinusoidal case will be much different than the spherical case as the

amount of deformation is increased. While the spherical case approaches a rod or cone type problem [22, 24], the sinusoidal case appears to reduce to a flat against a flat problem as interference increases and the sinusoidal surface is flattened out. Thus, it would appear that the hardness of the sinusoidal surface will initially stay constant or slightly decrease with interference (depending on the value of Δ/λ) and then eventually start increasing again as flattening occurs.

For sinusoidal surfaces with large values of Δ/λ , the hardness to yield strength ratio H/S_y will probably decrease initially because the geometry is very similar to that of a post or rod. However, for smaller values of Δ/λ , H/S_y will probably never decrease because the surface is more flat and the post or rod shape is never approached. Then, when the contact is more flat, the effective H/S_y becomes larger (as shown in the following sections). It should be noted that the surfaces simulated in this work are for fairly low values of Δ/λ , and so examples of the first case are never seen.

When the sinusoidal surface is almost completely flattened, one may initially conclude that the contact condition is similar to the spherical case at low a/R values and thus H/S_y returns to approximately 2.84 or higher values (as was concluded by Gao et al.[21]). However, if this case is examined closely, it becomes unclear what the actual limiting pressure is during the complete contact case. For example, once complete contact has occurred, the case becomes very similar to that of a compressed cavity of material (see Fig. 2.4). In this case the material cannot deform in the lateral direction parallel to the surface because there are neighboring identical sinusoidal contacts. During elastic contact and using Hooke's Law

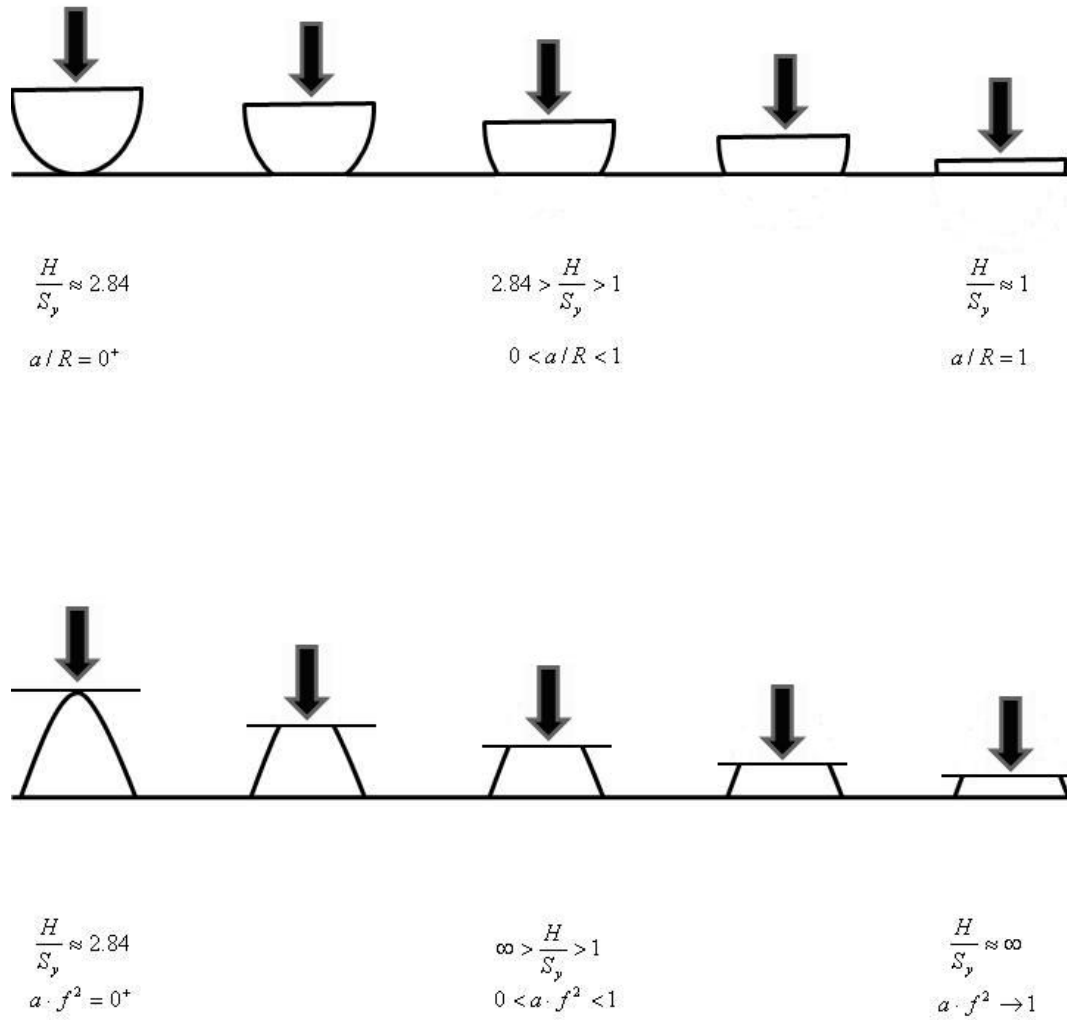


Figure 2.3: Diagram of the hypothetical progression of change in hardness with geometry for spherical and sinusoidal contact.

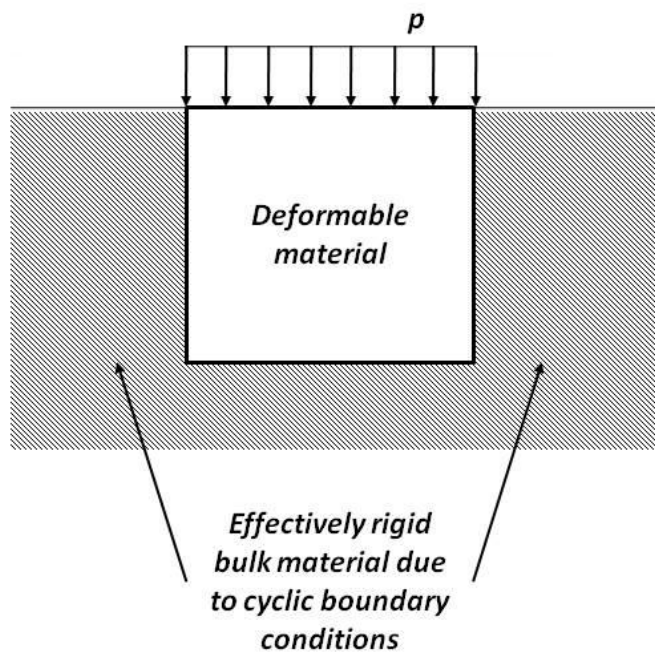


Figure 2.4: Compressed cavity of material.

the normal pressure is related to the lateral stresses by

$$\sigma_{lateral} = \frac{1 - 3\nu}{1 - \nu} P \quad (2.16)$$

However, the current case is not elastic, but it is unclear what the material does when large plastic deformations occur, or if it can reach the plastic regime once complete contact has occurred. One way to model a plastically deforming material is to assume that it conserves volume ($\nu = 0.5$) then $\sigma_{lateral} = -P$. For the cavity case, plastic deformation then cannot occur since the shape of the material is restricted, and so the only way for the material to deform is for it to compress volumetrically (hydrostatic stress). Thus the volume of material can only deform elastically and H/S_y approaches infinite values (see Fig. 2.4). In the work by Gao and Bower [18] and Gao et al. [21] it also appears that H/S_y increases dramatically when a loaded 2-D surface approaches the case of complete contact. However, in the current 3-D model the authors' find that p^* during fully plastic deformation is not limited by a value of $5.8 \cdot S_y$ that appears to limit the 2-D case [21].

Greenwood and Rowe [25] cover the topic of plastic crushing of serrated surfaces and also note that the force to cause complete contact becomes drastically larger as the surfaces come closer together. The case of a conical indenter correlates to this case as well, since as the angle of the cone tip approaches 180° the stress beneath the indenter will then become hydrostatic (see Marsh [26] and Johnson [27]). This is also a similar concept to that employed by the fractal contact models of Majumdar and Bhushan [28], in that they predict as the contact area increases, the contacting asperities will effectively become more elastic. However, it should be noted that in reality the material in the current case did initially undergo severe plastic deformation, so that even though the contact appears to behave

elastically near complete contact, it has undergone a large amount of plastic deformation to arrive at that condition.

2.5 Statistical contact model

Greenwood and Williamson [29] first introduced the statistical approaches for surface topography characterization in contact mechanics. This method has long been viewed as a simple and easy to use rough surface contact model. However the simplicity of this model has a few short comings such as the dependence of spectral moments on the resolution of the surface measuring apparatus and the sample length as shown by [30] and [31]. This dependence can skew the results for the contact parameters, such as the contact area and contact load, which depend on the surface parameters.

Greenwood and Williamson in their work [29] showed that rough surfaces can be modeled as a set of mutually exclusive asperities with constant radii and a variable height based on a particular height distribution function. The parameters that characterize the surfaces are the standard deviation of asperity heights σ_s , the areal asperity density η , and the asperity radius R . These parameters are a function of the spectral moments which are extracted from the surface using [32]. The value of σ_s is related to σ , η , R given by (Eq. 2.17).

$$\sigma_s^2 = \sigma^2 - \frac{3.717e^{-4}}{\eta^2 \cdot R^2} \quad (2.17)$$

A Gaussian distribution $\phi(z)$ is usually assumed for the height distribution. The contact parameters of rough surfaces are obtained as given by

$$A(d) = \eta A_n \int_d^\infty \bar{A}(z-d)\phi(z) dz \quad (2.18)$$

$$P(d) = \eta A_n \int_d^\infty \bar{P}(z-d)\phi(z) dz \quad (2.19)$$

where A_n is the nominal or apparent area of contact, which is defined by the overlap of surfaces in contact. The individual asperity contact area, \bar{A} , and the corresponding contact load \bar{P} , are functions of ω , which is the individual asperity interference. This original GW model assumes elastically deforming hemispherical asperites defined by Hertz solution [3]. Later models also expand the statistical methodology using elasto-plastic asperity contact models [22] and [33].

2.6 Fractal contact model

In order to overcome the drawback of spectral moments dependence on surface parameters in the statistical model, the fractal contact model proves beneficial in characterization of surface topography. The fractal geometry proposed by [30] has been utilized to characterize the surface topography in contact mechanics. Although the fractal contact model captures the surface topography in a multi-scale nature, it is important to note that not all engineering surfaces have profiles which exhibit fractal behavior.

The feature of finer and finer detail becoming apparent as the measurement length scale is reduced is a characteristic of the fractal model. Many authors [34], [35], have proposed to replace the asperity model concept by a description of a surface as a fractal. The trouble with the fractal model, apart from what as mentioned earlier is that there is no obvious way to solve the contact problem for two fractal surfaces, or for one fractal surface contacting a plane. The most widely accepted fractal theory is that due to Majumdar and Bhushan [36] in which the distribution of contact areas is tied to the distribution of ‘islands’ cut off from the surface by a given horizontal plane as shown in Fig. 2.5. Therefore, the contact area is simply a truncation of the fractal surface geometry and the plane. This is a classical quantity in fractal theory. Majumdar and Bhushan [36] replace the material in each island by a smooth parabolic asperity, this effectively defines a fractal distribution of asperities that can then be treated as in a conventional asperity model.



Figure 2.5: Islands defined by a horizontal section.

A typical fractal surface profile can be generated using the Weierstrass-Mandelbrot function [34]. A truncated two-variable fractal profile can be described as [34]

$$z(x, y) = L \left(\frac{G}{L}\right)^{d-2} \left(\frac{\ln \gamma}{M}\right)^{1/2} \sum_{m=1}^M \sum_{n=0}^{n_{max}} \cdot (\cos \phi_{m,n} - \cos \left[\frac{2\pi \gamma^n (x^2 + y^2)^{1/2}}{L} \cos(\arctan(y/x) - \frac{\pi m}{M}) + \phi_{m,n} \right]) \quad (2.20)$$

where L is the sample length, D is the fractal dimension, G is the fractal roughness, γ ($=1.5$) is a scaling factor, M is the number of superimposed ridges, n is a frequency index, with $n_{max} = \lceil \log(L/L_s/\log \gamma) \rceil$ represents the upper limit of n , where L_s is the cut-off length and $\phi_{m,n}$ is a random phase. Majumdar and Bhushan [36] have extensively used fractal methods to characterize surface topography and also in scale independent rough surface contact models. Kogut and Jackson [31] in the paper showed a series of results comparing short falls of the statistical and fractal models for rough surface contacts. To address these issues, several new multiscale models have been developed and are outlined in Chapter 5.

CHAPTER 3

FINITE ELEMENT MODEL

3.1 Introduction

This chapter describes in detail the methodology employed in building the solid finite element model. The solid model is divided into two parts. The first being the rigid flat plate that acts as the contact surface and the second being the sinusoidal surface on which target elements are created. Initially, the elastic case will be compared to the known solution to confirm the model accuracy. once verified the model will be given elastic perfectly plastic material properties.

3.2 Building the solid model

The current analysis will examine the case of three-dimensional elastic perfectly plastic sinusoidal contact by building on these previous works, using fundamental solid mechanics theory, and conducting a parametric study using the finite elements method. The sinusoidal surface considered by the current work is described by

$$h = \Delta \cdot \left(1 - \cos \left(\frac{2 \cdot \pi \cdot x}{\lambda} \right) \cos \left(\frac{2 \cdot \pi \cdot y}{\lambda} \right) \right) \quad (3.1)$$

and is shown (Fig. 2.1), where h is the height of the sinusoidal surface from its base. This is very similar to the surface used by Johnson et al. [1] and results in the same analytical equations for elastic contact.

A three-dimensional model was developed and the commercial *ANSYSTM* 8.1 package was used to further analyze the elasto-plastic sinusoidal contact problem. Owing to the symmetry of the sinusoidal surface (shown in Fig. 2.1 and 3.2), only a quarter section of the whole problem is modeled. The sinusoidal profile was generated based on equation (Eq. 3.1). Keypoints were created for various values of x , y , and h . These keypoints were then connected through lines. A conformal area was fit to generate the sinusoidal surface. In all, over 42,000 elements were used in the analysis. Solid45, which is an 8-node brick element, was used within the entire volume of the model. Contact174 and Target170 elements collectively formed the contact pair to model interaction between the surfaces.

3.3 Mesh convergence test

The number of elements was increased iteratively by a factor of 2 until mesh convergence was obtained. The final value corresponded to concordant values over two successive iterations. Upon final convergence the rigid flat surface, comprising of Contact174 elements, was a uniform mesh formed by a 21x21 array (Fig. 3.1) of elements. In all, there were approximately 1200 contact elements in the model. The contact stiffness value was also altered until the model agreed with the elastic solution (see section 3.5).

The uniform mesh on the rigid surface is used to predict the real contact area with the sinusoidal surface. By determining the contact status of each node during post-processing the total number of nodes in contact and the corresponding contact pressures are obtained from the nodal solution for incremented values of displacement. The ratio of the number of nodes in contact to the total number of nodes over the surface gives the real area of contact normalized by the apparent or nominal area of contact.

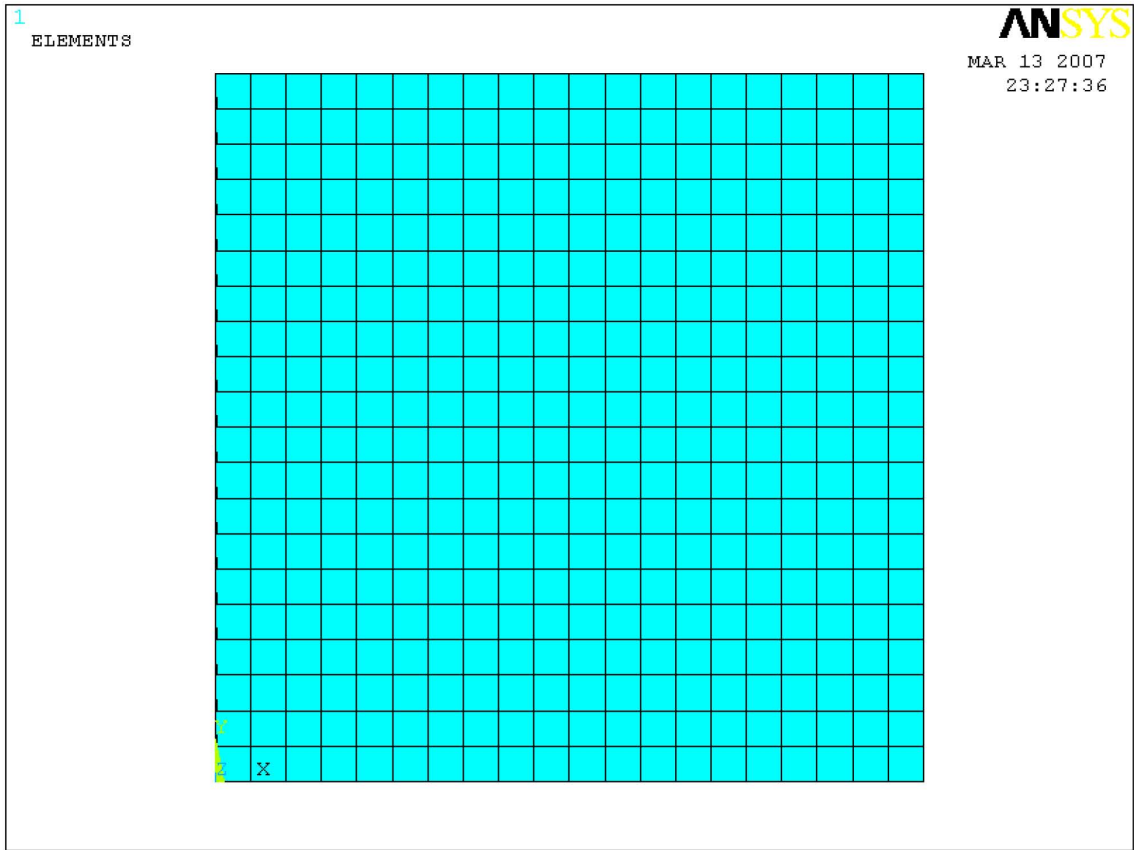


Figure 3.1: Uniform mesh on the rigid flat formed by 21x21 array of elements.

3.4 Simulation methodology

The displacement method was employed to simulate the contact problem. This method applies a finite displacement to the rigid flat surface in the z -direction toward the sinusoidal surface, and then solves the contact problem. This non-linear analysis accounts for large displacements, hence additional measures were taken to enable the non-linear geometry option during the course of the simulation. Displacement boundary conditions were enforced on the surface areas of the solid model, and not in the contact area (see Fig. 3.2). The base surface along the xy plane was fixed in all directions. The flat rigid surface was constrained to move only along the z axis. Constraints were applied to surfaces located on the xy , xz and yz planes in the direction perpendicular to the plane (thus enforcing a cyclic boundary condition). For example, a surface area along the yz planes was constrained in the x -direction, as shown in Fig. 3.2.

The simulation methodology can be understood better from Fig. 3.3. A contour of the displacement in the z -direction is plotted on the deformed sinusoidal structure for the elastic sinusoidal case. The material properties that were used to model this case is given in Table 3.1. The surface on which the zero displacement boundary conditions were imposed can be clearly seen during the course of simulation.

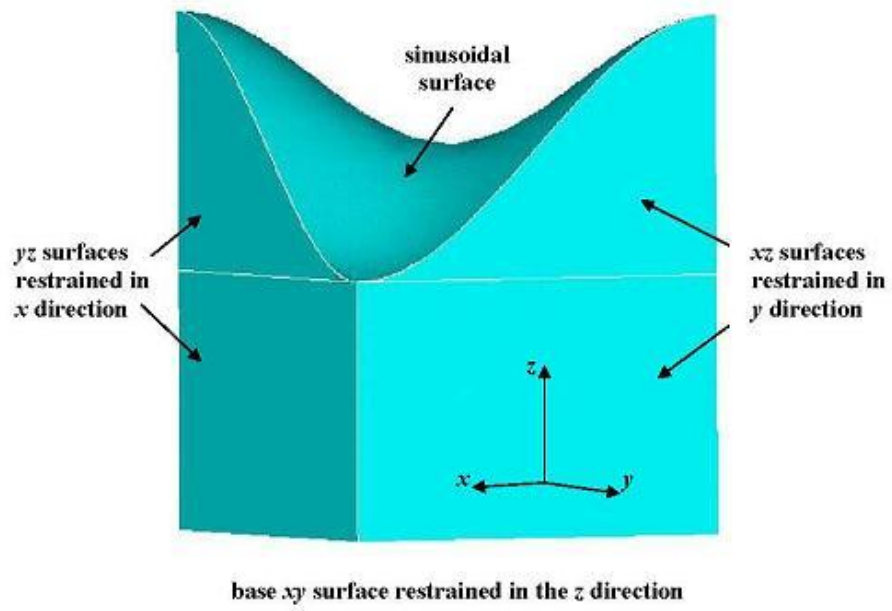


Figure 3.2: Schematic of degree of freedom restraints used for the one quarter sinusoidal FEM model (actual modeled geometry is much longer in the z direction).

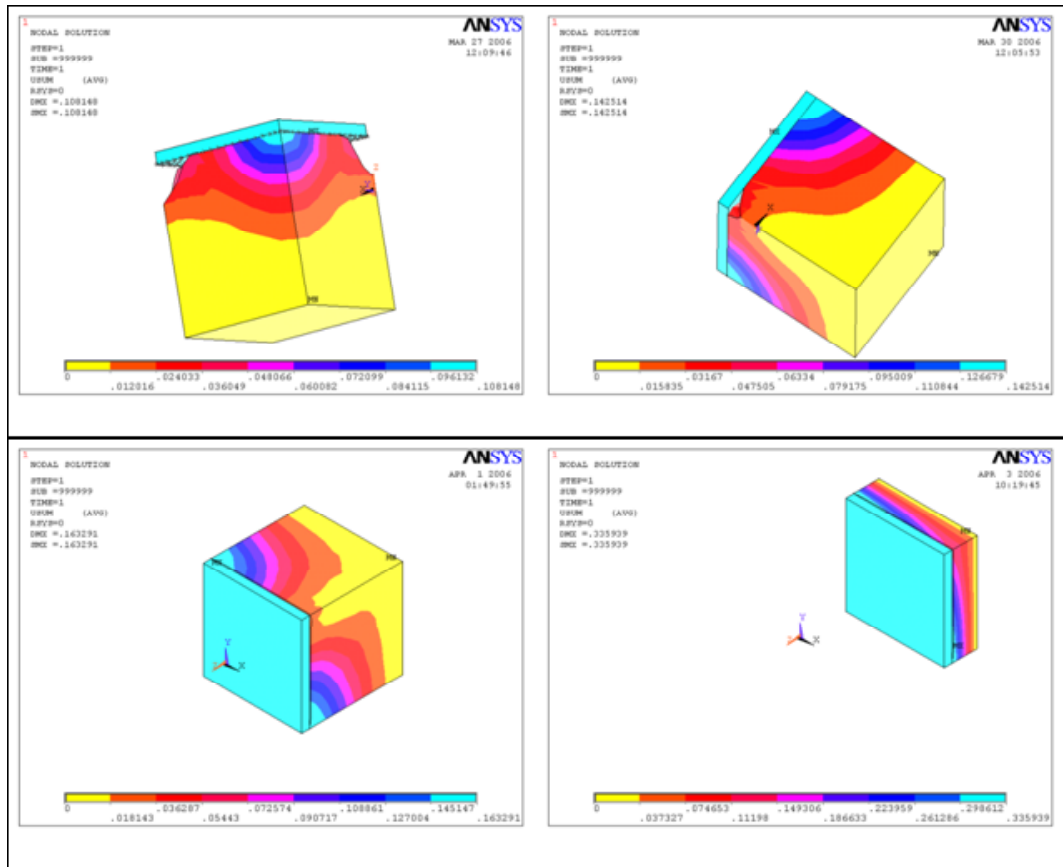


Figure 3.3: Various stages of contact.

The deformation history of the sinusoidal contact for the elasto-plastic benchmark case is shown in Fig. 3.4. The material properties used for the benchmark case are $E = 200GPa$, $S_y = 1GPa$, and $\nu = 0.3$. The dimensionless geometric ratio Δ/λ was set as 0.02. The contour plot (Fig. 3.4) represents the nodal displacements in the z -direction. Interpenetrations that were observed during the course of simulation runtime were well within accepted values of interference. Hence, these interpenetrations did not affect the finite element analysis results.

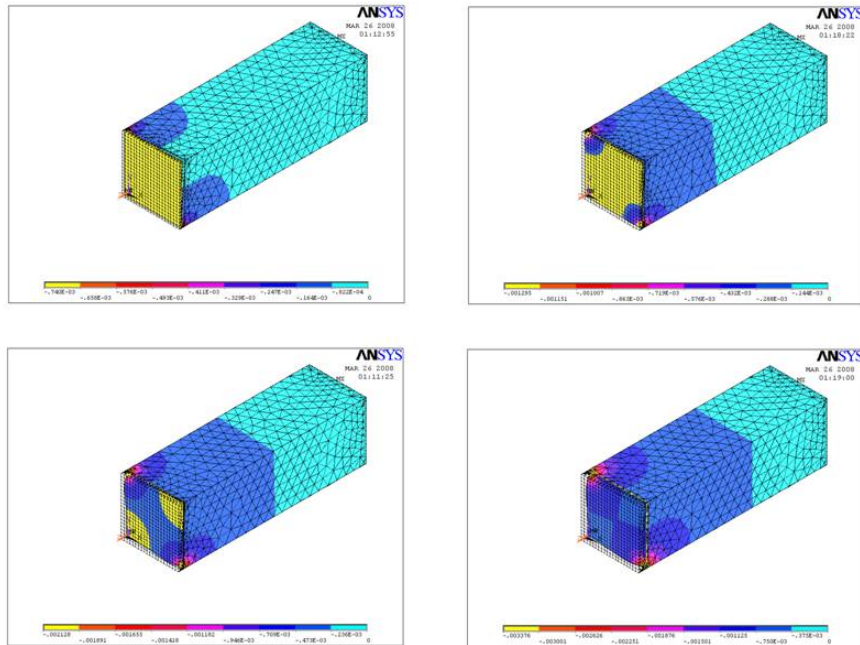


Figure 3.4: Deformation history.

3.5 Verification of model accuracy

Model accuracy was achieved by comparing the elastic results of the finite element model (FEM) to that of Johnson et al.'s data [1] (see Fig. 3.5). From Fig. 3.5, FEM data from the elastic sinusoidal case lie well within the two asymptotic solutions provided by Johnson et al. [1]. It is also clear that the curves for both the data sets followed almost identical paths. Table. 3.1 shows the parameters describing the JGH [1] data and the FEM results from the elastic sinusoidal model [13]. An average error of 6% was found to exist between the FEM and JGH data over the entire range of pressure.

Table 3.1: Material properties

Treatment	JGH data	FEM data
Young's Modulus E	200 <i>GPa</i>	200 <i>GPa</i>
Δ/λ	0.02	0.02
Average pressure for complete contact (p^*)	19.5 <i>GPa</i>	19.5 <i>GPa</i>

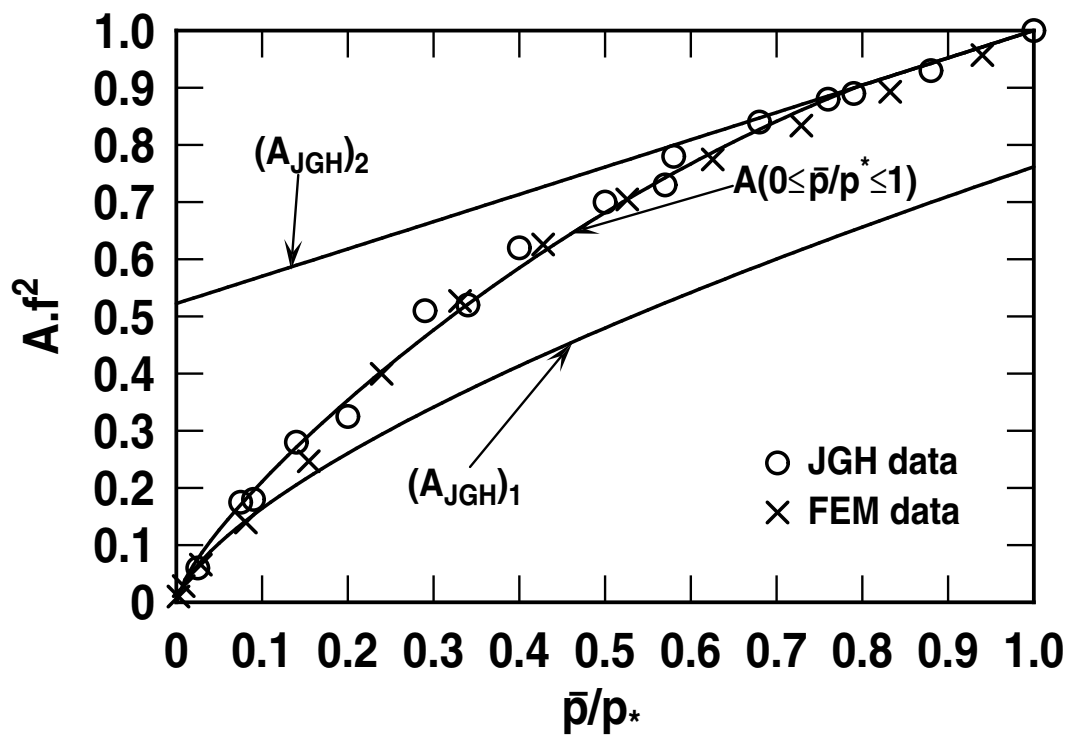


Figure 3.5: Comparison of elastic FEM results with JGH model.

CHAPTER 4

ELASTO-PLASTIC FEM RESULTS

4.1 Introduction

The material properties of the solid 3D model used to run the elastic case, were modified for the elasto-plastic case. To enhance convergence, as outlined by Brizmer et al. [37], the material of the sinusoidal surface was assumed elasto-plastic bi-linear isotropic hardening with a yield stress, S_y , of 1 GPa and a tangent modulus, E_T , 2% of the Young's modulus E . This isotropic hardening significantly improves the convergence without causing a significant change in the results.

4.2 Parametric study

In order to formulate a fit for the FEM contact pressure a parametric analysis of the elasto-plastic sinusoidal surface contact problem was conducted. A benchmark case was set to analyze the contact problem. The material properties used for the benchmark case are $E = 200GPa$, $S_y = 1GPa$, and $\nu = 0.3$. The material properties along with the Δ/λ ratio were then individually varied to perform a parametric study. First, a range of yield stresses were considered in the model (see Figs. 4.1 and 4.2). The yield strength was varied from $S_y = 0.75GPa$ to $S_y = 2.25GPa$.

First the results are presented as a plot of the average pressure divided by the yield strength, \bar{p}/S_y , as a function of the normalized area, $A \cdot f^2$ (see Fig. 4.1). As the area increases the contact is becoming more complete and the amount of deformation is increasing.

Table 4.1: Parametric study based on the Yield Strength S_y

S_y	S_y	Δ/λ	E'	S_y/E'	p^*	p_{ep}^*
$7.50 \cdot 10^8$	$7.5 \cdot 10^8$	0.02	$2.2 \cdot 10^{11}$	$3.41 \cdot 10^{-3}$	$1.95 \cdot 10^{10}$	$4.35 \cdot 10^9$
$1.00 \cdot 10^9$	$1.0 \cdot 10^9$	0.02	$2.2 \cdot 10^{11}$	$4.55 \cdot 10^{-3}$	$1.95 \cdot 10^{10}$	$5.00 \cdot 10^9$
$1.25 \cdot 10^9$	$7.5 \cdot 10^8$	0.02	$2.2 \cdot 10^{11}$	$5.69 \cdot 10^{-3}$	$1.95 \cdot 10^{10}$	$5.66 \cdot 10^9$
$1.50 \cdot 10^9$	$7.5 \cdot 10^8$	0.02	$2.2 \cdot 10^{11}$	$6.82 \cdot 10^{-3}$	$1.95 \cdot 10^{10}$	$6.31 \cdot 10^9$
$1.75 \cdot 10^9$	$7.5 \cdot 10^8$	0.02	$2.2 \cdot 10^{11}$	$7.96 \cdot 10^{-3}$	$1.95 \cdot 10^{10}$	$6.97 \cdot 10^9$
$2.00 \cdot 10^9$	$7.5 \cdot 10^8$	0.02	$2.2 \cdot 10^{11}$	$9.10 \cdot 10^{-3}$	$1.95 \cdot 10^{10}$	$7.63 \cdot 10^9$
$2.25 \cdot 10^9$	$7.5 \cdot 10^8$	0.02	$2.2 \cdot 10^{11}$	$1.02 \cdot 10^{-2}$	$1.95 \cdot 10^{10}$	$8.28 \cdot 10^9$

Traditionally this would be considered to be the fully plastic regime and the average pressure, \bar{p} , would be the hardness, H . As shown, the ratio of \bar{p}/S_y increases past the typical H/S_y value of 3 and even past the value of 5.8 found in [21] for 2-D sinusoidal surfaces in contact. This agrees with the earlier theory that the contact becomes more elastic as the contact area becomes more complete ($A \cdot f^2 \rightarrow 1$).

Next, the average contact pressure, \bar{p} , resulting from the elasto-plastic model was normalized using p^* . Then the normalized contact area $A \cdot f^2$ was plotted versus \bar{p}/p^* . It can be seen that the normalized contact area increases steadily as the yield strength decreases. It can be seen from Fig. 4.2 that for a $\bar{p}/p^* = 0.42$, the normalized contact area ratio is 1 for all the cases (the contact is complete). Thus for the elasto-plastic cases, complete contact occurs much earlier than when it occurs in elastic contact, as is intuitively expected. Although the trend captured partially resembles the perfectly elastic behavior, in order to find empirical expressions for the elasto-plastic case, the findings suggest that a new average pressure to cause complete contact during elasto-plastic contact, p_{ep}^* , can be found.

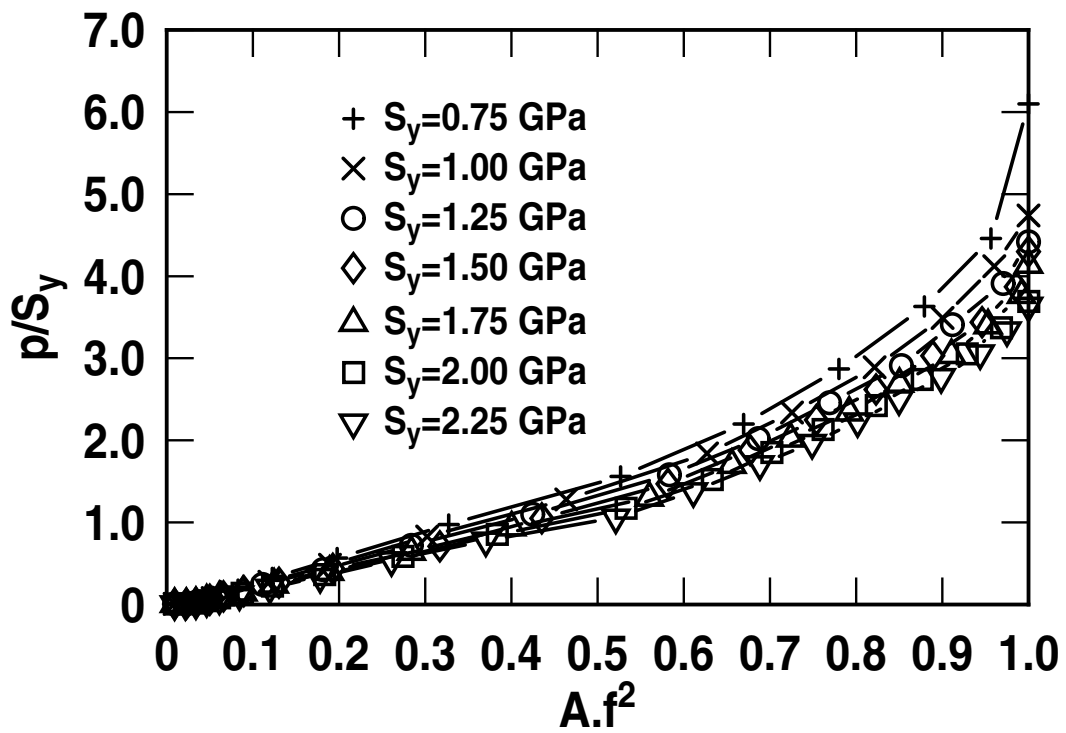


Figure 4.1: $\frac{p}{S_y}$ versus contact area ratio ($A \cdot F^2$) for different yield strength.

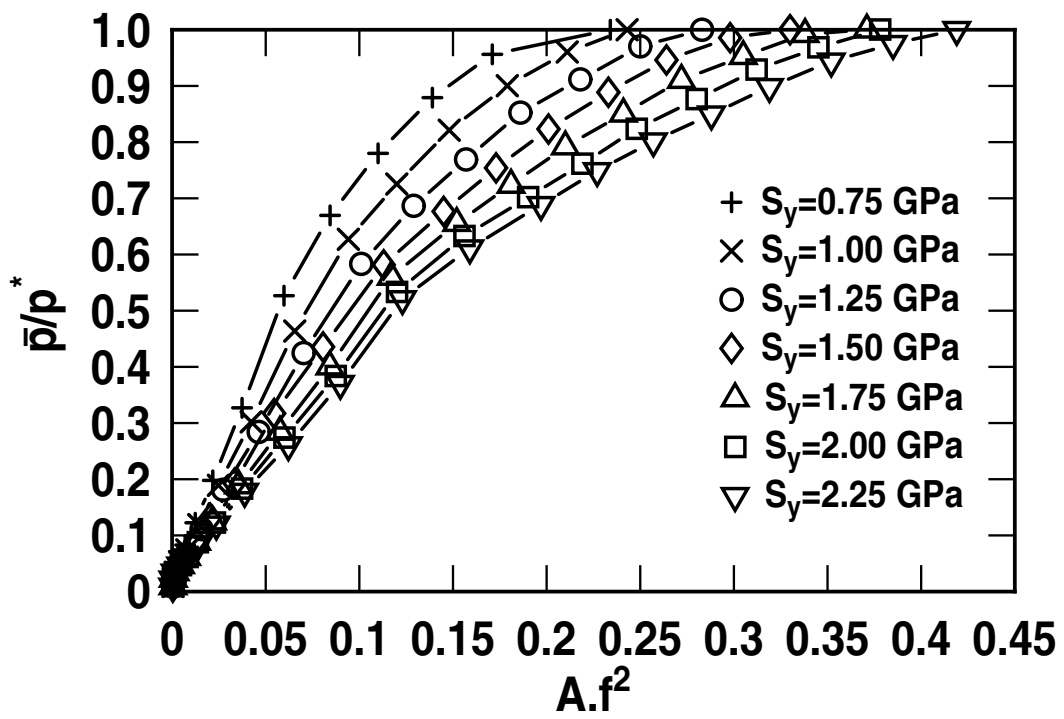


Figure 4.2: Contact area ratio ($A \cdot F^2$) versus \bar{p}/p^* for different yield strength.

Table 4.2: Parametric study based on the Young's Modulus E'

E'	S_y	Δ/λ	E'	S_y/E'	p^*	p_{ep}^*
$1.50 \cdot 10^{11}$	$1.00 \cdot 10^9$	0.02	$1.65 \cdot 10^{11}$	$6.07 \cdot 10^{-3}$	$1.46 \cdot 10^{10}$	$4.41 \cdot 10^9$
$2.00 \cdot 10^{11}$	$1.00 \cdot 10^9$	0.02	$2.20 \cdot 10^{11}$	$4.55 \cdot 10^{-3}$	$1.95 \cdot 10^{10}$	$5.00 \cdot 10^9$
$2.50 \cdot 10^{11}$	$1.00 \cdot 10^9$	0.02	$2.75 \cdot 10^{11}$	$3.64 \cdot 10^{-3}$	$2.44 \cdot 10^{10}$	$5.60 \cdot 10^9$
$3.00 \cdot 10^{11}$	$1.00 \cdot 10^9$	0.02	$3.30 \cdot 10^{11}$	$3.03 \cdot 10^{-3}$	$2.93 \cdot 10^{10}$	$6.20 \cdot 10^9$
$3.50 \cdot 10^{11}$	$1.00 \cdot 10^9$	0.02	$3.85 \cdot 10^{11}$	$2.60 \cdot 10^{-3}$	$3.42 \cdot 10^{10}$	$6.79 \cdot 10^9$

Table 4.3: Parametric study based on the Geometric ratio Δ/λ

Δ/λ	S_y	Δ/λ	E'	S_y/E'	p^*	p_{ep}^*
0.010	$1.00 \cdot 10^9$	0.010	$2.20 \cdot 10^{11}$	$4.55 \cdot 10^{-3}$	$9.76 \cdot 10^9$	$3.54 \cdot 10^9$
0.015	$1.00 \cdot 10^9$	0.010	$2.20 \cdot 10^{11}$	$4.55 \cdot 10^{-3}$	$1.35 \cdot 10^{10}$	$4.30 \cdot 10^9$
0.020	$1.00 \cdot 10^9$	0.020	$2.20 \cdot 10^{11}$	$4.55 \cdot 10^{-3}$	$1.95 \cdot 10^{10}$	$5.00 \cdot 10^9$
0.032	$1.00 \cdot 10^9$	0.032	$2.20 \cdot 10^{11}$	$4.55 \cdot 10^{-3}$	$3.12 \cdot 10^{10}$	$6.33 \cdot 10^9$
0.040	$1.00 \cdot 10^9$	0.040	$2.20 \cdot 10^{11}$	$4.55 \cdot 10^{-3}$	$3.91 \cdot 10^{10}$	$7.08 \cdot 10^9$

4.3 Critical elasto-plastic pressure estimation

The average pressure, p_{ep}^* , that causes complete contact is extracted from the finite element model data for each modeled case. This value corresponds to the average pressure when the area ratio, $A/f^2 = 1$. At this stage complete contact occurs between the rigid flat and the sinusoidal surface. An equation is fit to the values of p_{ep}^* from the finite element data. The goal of the empirical fit is to obtain a single expression that takes into consideration both the material and geometric properties of the modeled elasto-plastic sinusoidal contact problem. Since the material properties and geometric properties are each varied independently from the benchmark case, an equation can easily be fit to each trend. It was also found that the effects S_y and E' appear to be almost exactly inverse and can be combined into one normalized variable S_y/E' . The resulting equation fit to the FEM data is given as

$$\frac{p_{ep}^*}{p^*} = \left(4.172 \cdot \frac{S_y}{E'} + 0.0173 \right) \cdot \sqrt{\frac{\lambda}{\Delta}} \quad (4.1)$$

The effect of S_y/E' on p_{ep}^*/p^* is shown by the plot in Fig. 4.3. The relationship of p_{ep}^*/p^* to S_y/E' appears to be linear in nature. As shown in Fig. 4.3, Eq. 4.1 differs from the FEM data by an average error of 3.82% with the maximum and minimum errors being 7.89% and 0.17% respectively. The empirical fit generated thus seems to be effective.

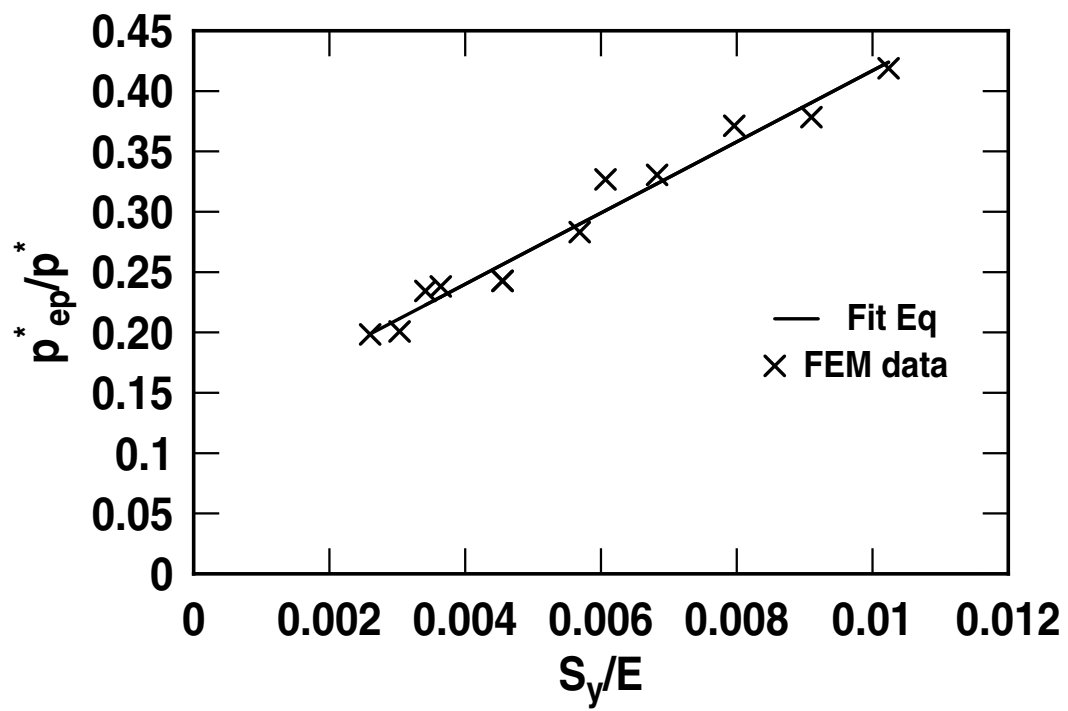


Figure 4.3: The effect of S_y/E' on pressure to cause complete contact.

Table 4.4: Variation of $\frac{p_{ep}^*}{p^*}$ (FEM) and $\frac{p_{ep}^*}{p^*}$ (Fit Eq. 4.1) with respect to S_y/E'

S_y/E'	Δ/λ	$\frac{p_{ep}^*}{p^*}$ (FEM)	$\frac{p_{ep}^*}{p^*}$ (Fit Eq. 4.1)	Error
$3.41 \cdot 10^{-3}$	0.02	0.2344	0.2226	4.9936
$4.55 \cdot 10^{-3}$	0.02	0.2429	0.2562	5.5666
$5.69 \cdot 10^{-3}$	0.02	0.2832	0.2897	2.3355
$6.82 \cdot 10^{-3}$	0.02	0.3305	0.3233	2.1570
$7.96 \cdot 10^{-3}$	0.02	0.3712	0.3568	3.8621
$9.10 \cdot 10^{-3}$	0.02	0.3784	0.3904	3.1821
$1.02 \cdot 10^{-2}$	0.02	0.4189	0.4240	1.2284
$6.07 \cdot 10^{-3}$	0.02	0.3268	0.3009	7.8912
$4.55 \cdot 10^{-3}$	0.02	0.2429	0.2562	5.4853
$3.64 \cdot 10^{-3}$	0.02	0.2382	0.2293	3.7062
$3.03 \cdot 10^{-3}$	0.02	0.2009	0.2114	5.2895
$2.60 \cdot 10^{-3}$	0.02	0.1983	0.1987	0.1769
			Average Error	3.8228

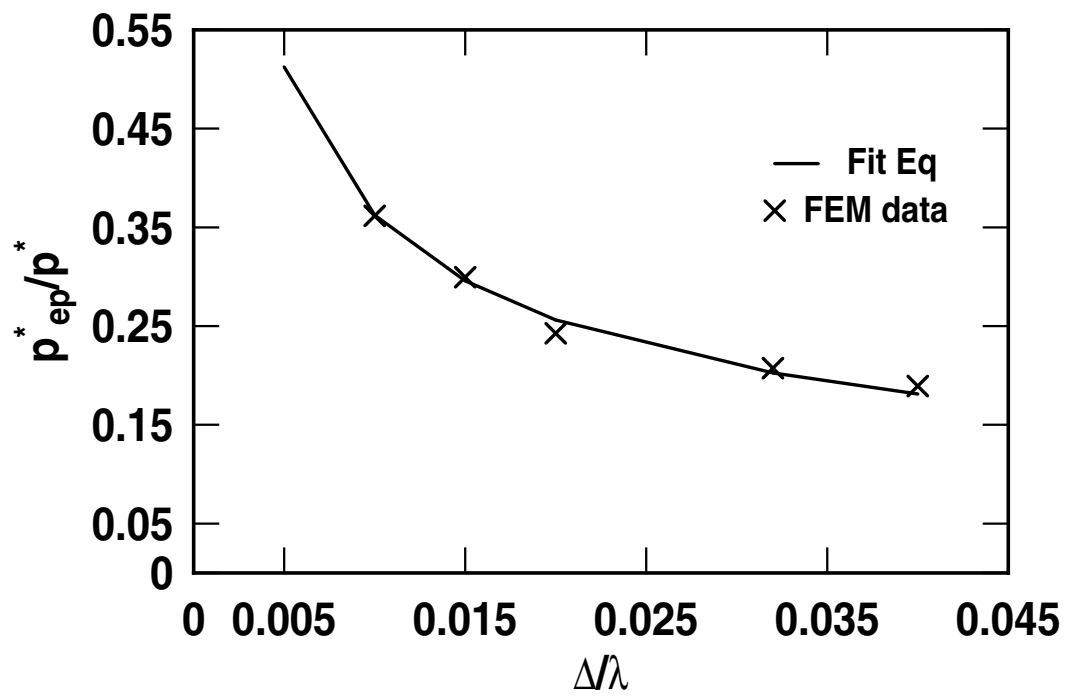


Figure 4.4: The effect of Δ/λ on pressure to cause complete contact.

Table 4.5: Variation of $\frac{p_{ep}^*}{p^*}$ (FEM) and $\frac{p_{ep}^*}{p^*}$ (Fit Eq. 4.1) with respect to Δ/λ

S_y/E'	Δ/λ	$\frac{p_{ep}^*}{p^*}$ (FEM)	$\frac{p_{ep}^*}{p^*}$ (Fit Eq. 4.1)	Error
$4.55 \cdot 10^{-3}$	0.010	0.3615	0.3623	0.2340
$4.55 \cdot 10^{-3}$	0.015	0.2995	0.2958	1.2202
$4.55 \cdot 10^{-3}$	0.020	0.2427	0.2562	5.5666
$4.55 \cdot 10^{-3}$	0.032	0.2027	0.2025	2.3742
$4.55 \cdot 10^{-3}$	0.040	0.1892	0.1811	4.2418
			Average Error	2.7274

The effect Δ/λ has on p_{ep}^*/p^* appears to be non-linear, as shown in Fig. 4.4. The p_{ep}^*/p^* value also decreases with an increase in the Δ/λ ratio. As apparent in Eq. 4.1, a square root function appears to produce a reasonable fit. The average error resulting from the fit is 2.72%, with maximum and minimum error values of 5.56% and 0.23% respectively.

Next the p_{ep}^* values obtained from Eq. 4.1 are used as a normalization factor for the contact pressure, \bar{p} , predicted by the elasto-plastic FEM model (see Figs. 4.5- 4.7). This normalization is useful because it is successful at collapsing the curves onto almost the same curve (see Fig. 4.5 in comparison to Fig. 4.2). Since similar plots are not shown for the results when E and Δ/λ are varied, the values are varied by as much as 100.5% between the E cases and 91.1% between the Δ/λ cases, which is large in comparison to the error values given above. The results for the cases of various yield strengths, S_y , are shown in the plot of $A \cdot f^2$ versus in Fig. 11. In this case the equivalent elastic modulus, $E' = 220GPa$ and the geometric property $\Delta/\lambda = 0.02$ are held constant for all the cases modeled. From a lower S_y value of 0.75 GPa to a higher value of 2.25 GPa the values of curves seem to increase slightly. As the yield strength, S_y , increases the curves appear to converge to a single curve. Towards complete contact it can be seen that although the curves are for different yield strengths, they converge to the same point due to the normalization by p_{ep}^* .

Since the trend of the normalized contact area $A \cdot f^2$ as a function of \bar{p}/p_{ep}^* should always begin at $A \cdot f^2 = 0, \bar{p}/p_{ep}^* = 0$ (just before initial contact) and end at $A \cdot f^2 = 1, \bar{p}/p_{ep}^* = 1$ (when complete contact occurs), the normalization is successful just at collapsing these end points together. However, the curvature of the normalized trend can still depend on the material and geometric properties. Therefore, additional measures are taken to fit equations to the FEM data.

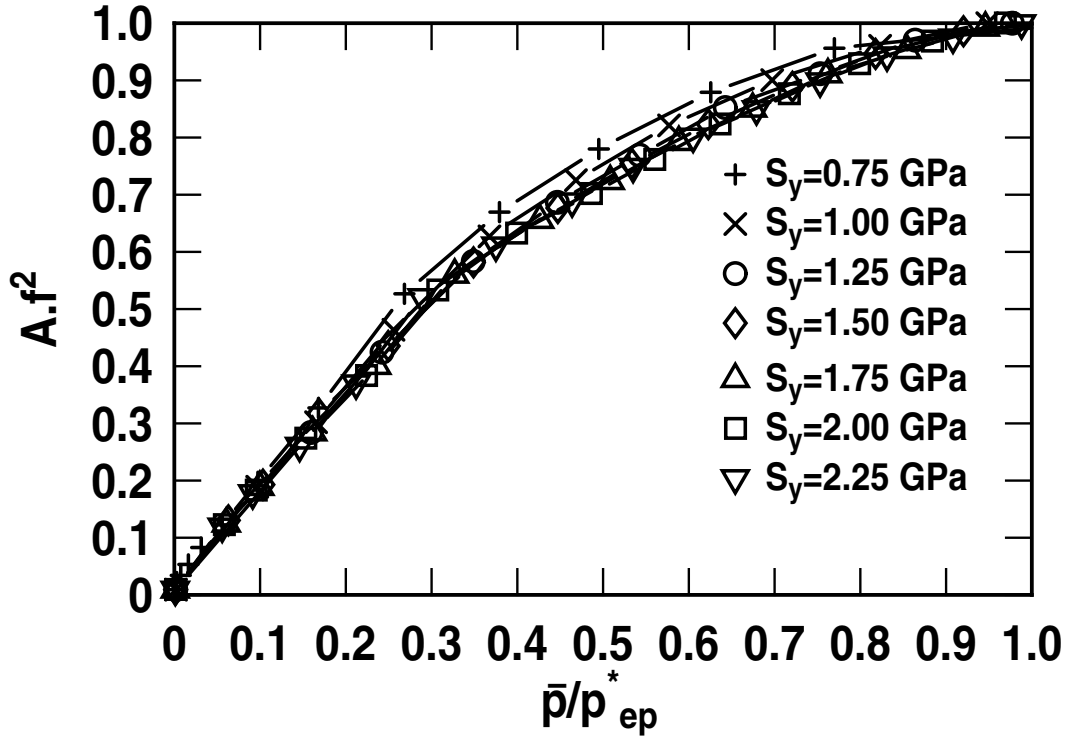


Figure 4.5: Contact area ratio ($A \cdot f^2$) versus \bar{p}/p_{ep}^* for different yield strength values.

From Fig. 4.6 it is seen that the elastic modulus E' and the yield strength S_y both display similar trends. This case is modeled by varying only the equivalent elastic modulus, E' , while the yield strength, $S_y = 1$ GPa and $\Delta/\lambda = 0.02$ are held constant for all the different

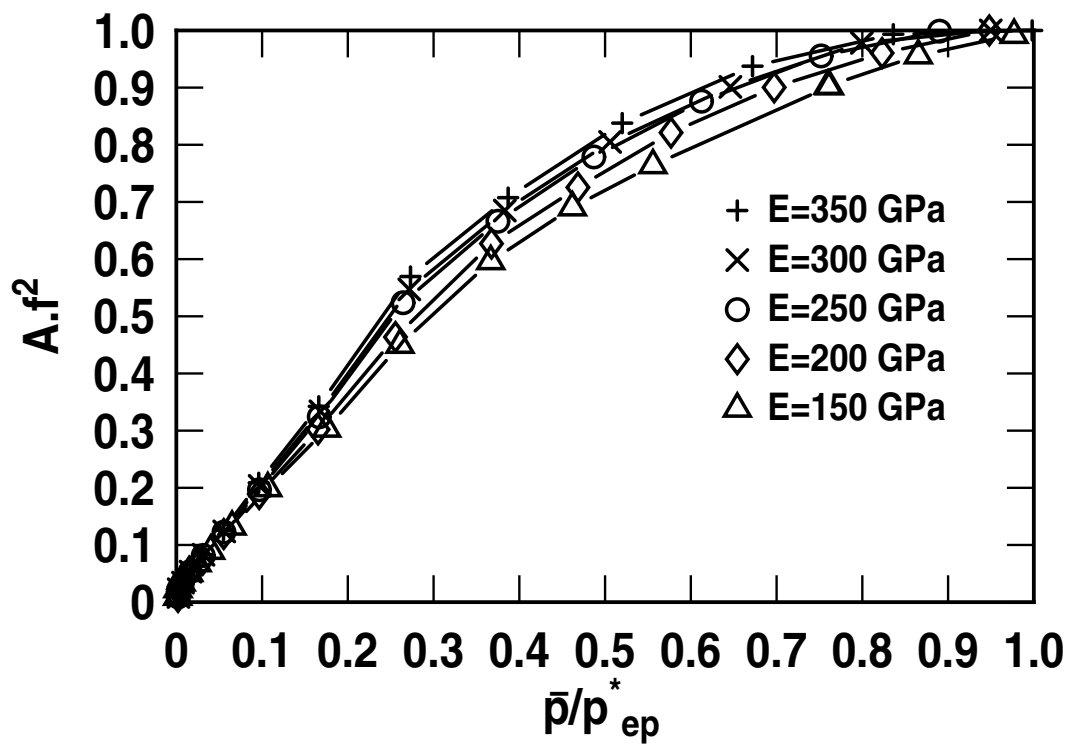


Figure 4.6: Contact area ratio ($A \cdot f^2$) versus \bar{p}/p_{ep}^* for different values of Young's Modulus E .

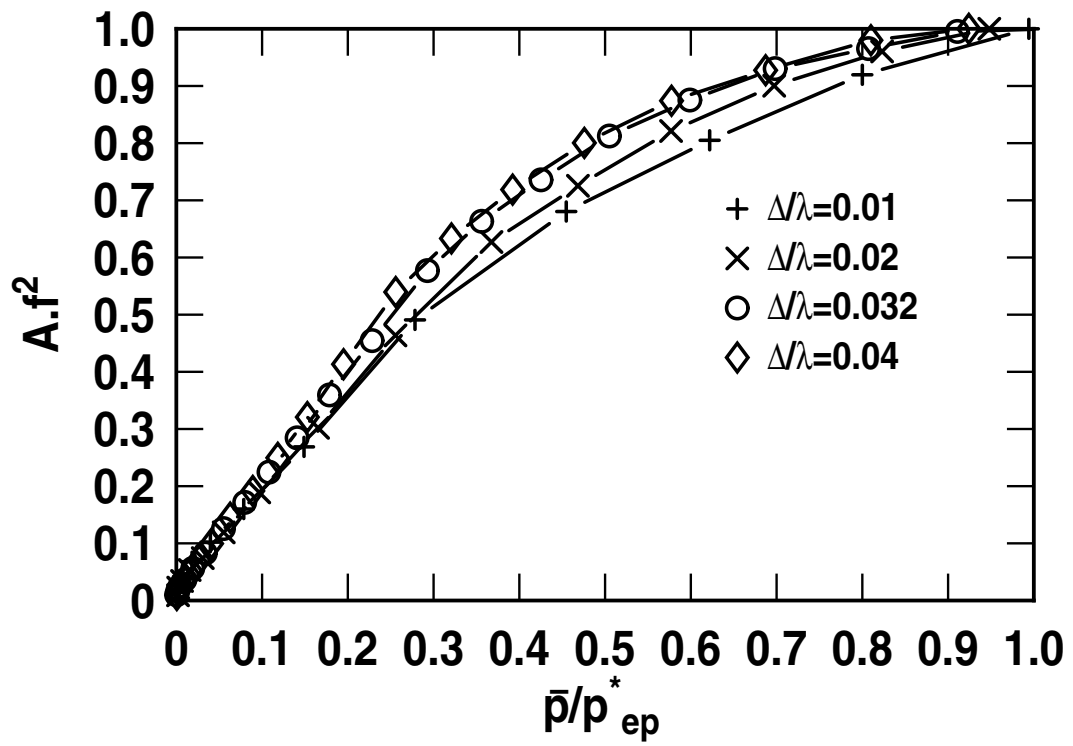


Figure 4.7: Contact area ratio ($A \cdot f^2$) versus \bar{p}/p_{ep}^* for different values of the dimensionless geometric quantity Δ/λ .

cases. As the elastic modulus increases, the curve also increases. At lower values of \bar{p}/p_{ep}^* the curves seem to fall onto a single curve. When the \bar{p}/p_{ep}^* value reaches 0.1 the curves seem to diverge. Near complete contact the curves converge again.

The geometric property Δ/λ is now varied from 0.01 to 0.04, as shown in Fig. 4.7. The equivalent modulus $E'=220$ GPa and the yield strength, $S_y=1$ GPa, are held constant in these various cases that are modeled. The contact pressure, \bar{p} , from the FEM data is again normalized by the average pressure for complete elasto-plastic contact, p_{ep}^* . This ratio is then plotted versus the contact area ratio. It can be seen that normalized area (Af^2) steadily increases when the Δ/λ ratio increases. Another point should be noted, that the lower values of the ratio Δ/λ allow for the solution to converge faster, while some higher values of Δ/λ do not converge at all. The reason for this dependence on Δ/λ for convergence could be from the fact that with higher Δ/λ ratios larger deformations are required to flatten out the sinusoidal surface.

4.4 Real contact area estimation

The area described by the KE model is next modified to better suit the current elasto-plastic sinusoidal contact problem. The premise for the argument is based on the fact that when $A/A_c=1$, the pressure to critical pressure ratio p/p_c should equal 1. Notice that p is now used to denote the average contact pressure over the contact area, while \bar{p} denotes the average pressure over the entire surface area. Based on the KE model, a logical function to model initial elasto-plastic contact is described below

$$\frac{A}{A_c} = \left(\frac{p}{p_c} \right)^d \quad (4.2)$$

where p_c from Eq. (A5) in Appendix 1 is

$$p_c = \left(\frac{2 \cdot C \cdot S_y}{3} \right)$$

substituting this into Eq. 4.2 we get,

$$\frac{A}{A_c} = \left(\frac{p}{2 \cdot C \cdot S_y} \cdot 3 \right)^d \quad (4.3)$$

where average pressure over the contact area, p , in Eq. 4.3 is converted to the average pressure over the entire surface, \bar{p} , by

$$p = \left(\frac{\bar{p} \cdot \lambda^2}{2 \cdot A} \right) \quad (4.4)$$

By substituting in Eq. 4.4 into Eq. 4.3 the following expression results

$$\frac{A}{A_c} = \left(\frac{\bar{p} \cdot \lambda^2 \cdot 3}{4 \cdot S_y \cdot C \cdot A} \right)^d \quad (4.5)$$

Solving for A in Eq. 4.5, one obtains the modified expression for contact area, which is now termed as A_{ep} . Also noting that the two sphere-like peaks occur in the λ^2 area of sinusoidal contact than a factor of two must be included. The result is given by

$$A_{ep} = 2(A_c)^{\frac{1}{1+d}} \left(\frac{3 \cdot \bar{p}}{4 \cdot C \cdot S_y} \lambda^2 \right)^{\frac{d}{1+d}} \quad (4.6)$$

Although this expression (Eq. 4.6) for area is derived differently, it is interesting to note that it is a similar result to the area to pressure relation from the KE model (Eq. 2.10).

The value of d is obtained empirically by fitting a curve to the FEM results. To allow a good fit with the FEM results, the value of d found in Eq. 4.6 for A_{ep} is allowed to vary with E'/S_y and Δ/λ . The expression for d is given by

$$d = C_1 \cdot \left(\frac{E'}{S_y} \cdot \frac{\Delta}{\lambda} \right)^{C_2} \quad (4.7)$$

where, $C_1 = 3.8$ and $C_2 = 0.11$ and are constants which are obtained empirically. E' and S_y are the effective Young's modulus and yield strength respectively. For the benchmark case of $E'=220$ GPa, $S_y=1$ GPa, and $\Delta/\lambda=0.02$, then $d=4.47$. As expected, this is close to the value of 4.93 that is predicted by the KE model.

To model the contact area as a function of load, the results of Jackson and Streator [14] are now modified with the elasto plastic results now given by Eqs. (4.1and 4.6). The modified version of the model to consider elasto-plastic deformation is

$$A = (A_{ep}) \left(1 - \left[\frac{\bar{p}}{p_{ep}^*} \right]^{1.51} \right) + (A_{JGH})_2 \left(\frac{\bar{p}}{p_{ep}^*} \right)^{1.04} \quad (4.8)$$

where A_{ep} is the spherical elasto-plastic contact area as predicted by the model given by Eqs. (4.6 and 4.7) and based on the KE model. Then as the load increases, the contact will diverge from the spherical case and asymptotically approach the sinusoidal case. Since the H/S_y will theoretically increase as the contact becomes more complete (see previous discussion concerning Fig. 2.4), the contact area may theoretically approach the elastic limit $(A_{JGH})_2$ as \bar{p}/p_{ep}^* approaches 1. However, when the solution approaches $(A_{JGH})_2$ the average pressure is p_{ep}^* instead of p^* as in the elastic case. Also, if A , as predicted by Eq. 4.8, increases past λ^2 then $A=\lambda^2$.

4.5 The empirical model

The FEM results are presented alongside the model given by Eq. 4.8 in Figs. 4.8, 4.9, and 4.10. In Fig. 4.8 we see the fit between the two extreme cases that were modeled based on the yield strength of the material. The lowest S_y value considered being 0.75 GPa and the higher value being 2.25 GPa. We can see clearly that the modified KE model for contact area agrees reasonably well with the numerical results. The average error between the new model given by Eq. 4.8 and the FEM results when the yield strength is varied independently is less than 5%.

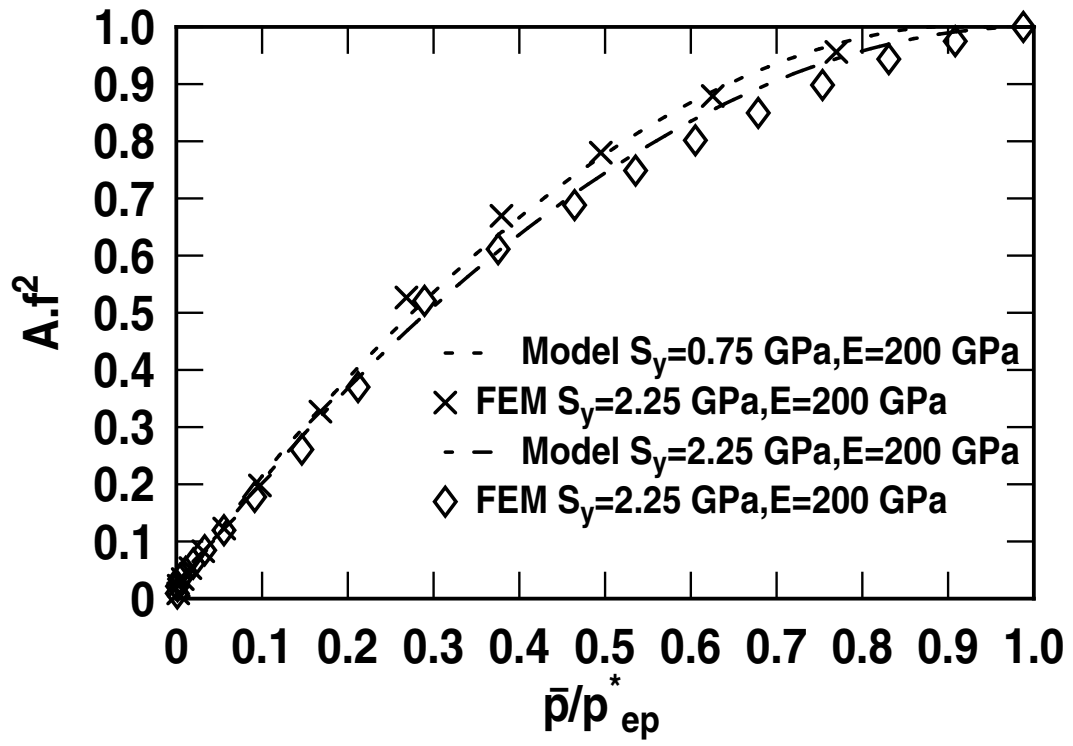


Figure 4.8: Comparison of the FEM results and the elasto-plastic sinusoidal contact model (marked by lines) given by Eq. 4.8 for different yield strength values.

Likewise, the plots in Fig. 4.9 and 4.10 show that the model also compares well for the cases where the elastic modulus, E , and the geometry, Δ/λ , are varied (the error in these cases is also less than 5%). Fig. 4.9 a comparison of the FEM results and the elasto-plastic sinusoidal contact model (marked by lines) given by Eq. 4.8 for different Young's modulus values is shown. Similarly in Fig. 4.10 a comparison of the FEM results and the elasto-plastic sinusoidal contact model (marked by lines) given by Eq. 4.8 for different sinusoidal geometries is shown.

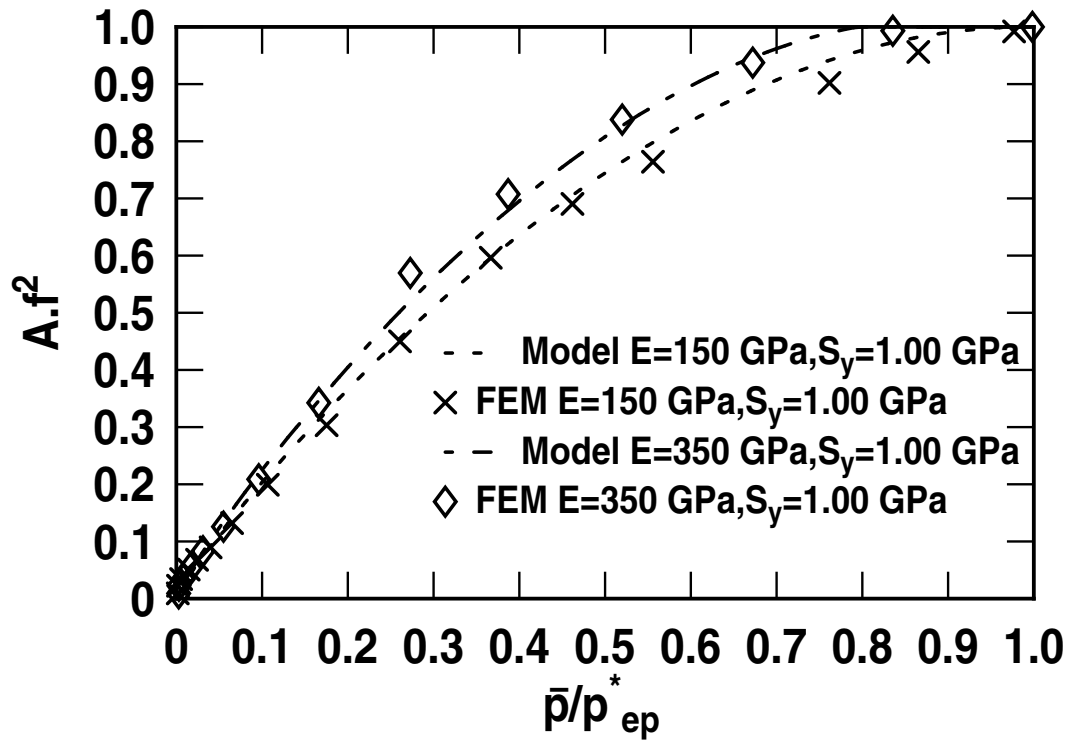


Figure 4.9: Comparison of the FEM results and the elasto-plastic sinusoidal contact model (marked by lines) given by Eq. 4.8 for different Young's modulus values.

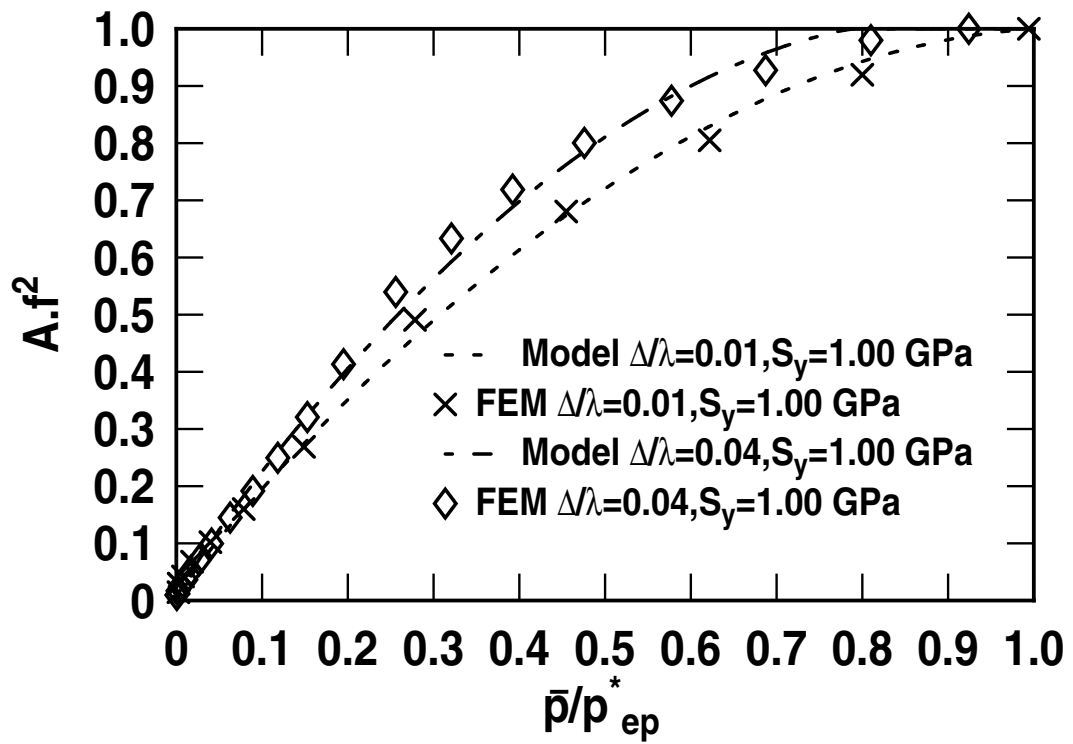


Figure 4.10: Comparison of the FEM results and the elasto-plastic sinusoidal contact model (marked by lines) given by Eq. 4.8 for different sinusoidal geometries.

CHAPTER 5

MULTISCALE ROUGH SURFACE CONTACT MODEL

5.1 Introduction

In this chapter a non-statistical multiscale model using the elastic and elasto-plastic sinusoidal contact, based on the work by Jackson and Streater [14], is presented. The equations generated empirically using FEM in earlier chapter's are included in the formulation of the multiscale model. This model incorporates the effect of asperity deformations at multiple scales into a simple foundation for modeling rough surfaces. This model considers the effect of having smaller asperities located on top of larger asperities in repeated fashion, very similar to the "protuberance upon protuberance" theory proposed by Archard [40].

5.2 Multiscale model foundation

The current multiscale model uses the same direction as Archard [40], but differs in the ease of use when applied to real rough surfaces. The model assumptions derived from Jackson and Streater [14], which are different from the statistical and fractal models, are as follows:

1. Asperities are stacked so that smaller asperities (higher frequency) are on top of larger asperities (lower frequency).
2. Each iteration or frequency level of asperities carries the same total load.
3. The load is shared equally among all the asperities at a given frequency level.

4. At a given frequency level, each asperity deforms according to Hertz theory or to a chosen elasto-plastic asperity contact model, irrespective of the presence of higher frequency asperities upon it. In the current work the sinusoidal contact models will be used.
5. At a given frequency level the contact area cannot increase beyond what is experienced by the frequency level below it.

These assumptions set up the following foundation of equations for the contact model:

$$A_r = \left(\prod_{i=1}^{i_{max}} \bar{A}_i \eta_i \right) A_n \quad (5.1)$$

$$F = \bar{F}_i \eta_i A_{i-1} \quad (5.2)$$

where A_r is the real area of contact, F the contact load, A_n the nominal contact area, and the subscript i denotes a frequency level, with i_{max} denoting the highest frequency level considered. A flow chart of the method is given by Fig. 5.1. This illustrates how the contact model foundation is used to model the contact between rough surfaces. First FFT of the acquired surface data is performed. If a spherical contact model is used to consider individual asperity, the areal density and radius of curvature are computed for each frequency level from the resulting Fourier series. Although in the current work these quantities are not used, they can be computed as follows:

$$\eta_i = 2f_i^2 \quad (5.3)$$

$$R_i = \frac{1}{4\pi^2\beta_i f_i^2} \quad (5.4)$$

where β_i is the amplitude at the given frequency level and f_i is the frequency. The source of factor two is from [1]. This factor only means that there are two density of asperity peaks per reference area. However, the above methodology differs when a sinusoidal contact model is used. because the amplitude and wavelength can be directly used from the FFT. By using the sinusoidal contact model assumption 5 will also never be violated. The nominal contact area A_n is defined at the zeroth frequency level or at $i = 0$. For a chosen level of frequencies, the number of asperities is calculated for every frequency level. At a given level the total load is then equally divided among all the asperities of that level. From the given asperity load, dimension, the material property and the chosen deformation model, the single asperity area is determined. A temporary total contact area for the given frequency level is computed by multiplying the number of asperities at that level. Assumption 5 mentioned above is then verified at every frequency level. If the contact area predicted at that level is greater than the contact area at frequency level below it, the smaller contact area serves as the nominal contact area for the given frequency level. This procedure is repeated iteratively until all the frequency levels are considered, resulting in a prediction of the real contact area as a function of applied load.

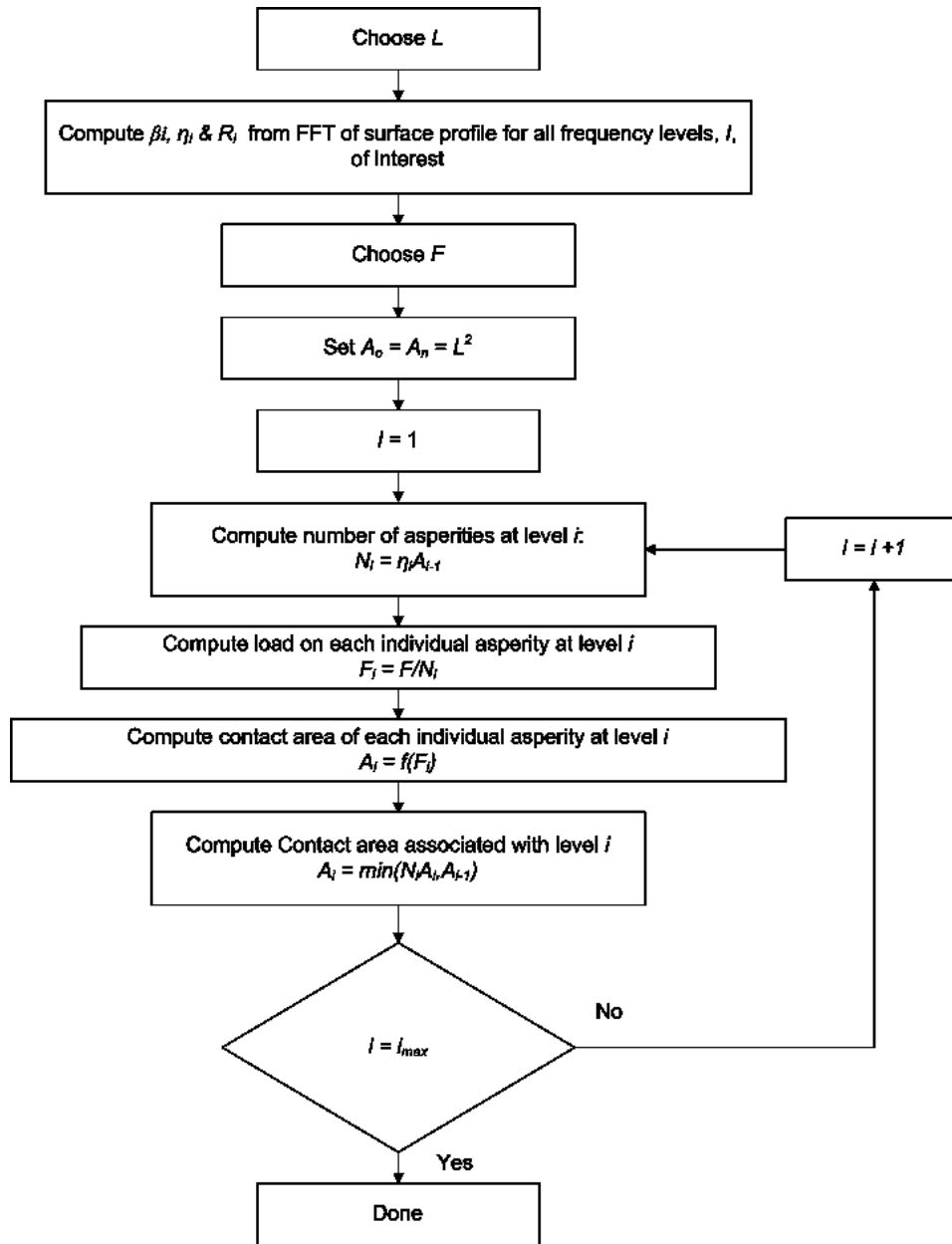


Figure 5.1: Flow chart of iterative asperity contact model.

5.3 Elasto-plastic multiscale model

The sinusoidal asperity model developed earlier is used within the multiscale model foundation described above to relate the contact area to the applied load. The modified KE contact area is used to define the asperity deformation model. A_{ep} is given by

$$A_{ep} = 2(A_c)^{\frac{1}{1+d}} \left(\frac{3 \cdot \bar{p}}{4 \cdot C \cdot S_y} \lambda^2 \right)^{\frac{d}{1+d}} \quad (5.5)$$

To model the contact area as a function of load inside the multi-scale model foundation, the JGH contact area is modified with the elasto plastic results now given by Eqs. (4.1and 5.5). The modified version of the model to consider elasto-plastic deformation is

$$A = (A_{ep}) \left(1 - \left[\frac{\bar{p}}{p_{ep}^*} \right]^{1.51} \right) + (A_{JGH})_2 \left(\frac{\bar{p}}{p_{ep}^*} \right)^{1.04} \quad (5.6)$$

where A_{ep} is the spherical elasto-plastic contact area as predicted by the model given by Eqs. (5.5 and 4.7) and based on the KE model. Then as the load increases, the contact will diverge from the spherical case and asymptotically approach the sinusoidal case. A limiting condition for elastic sinusoidal case was provided by Johnson et al. [1].

5.4 Frequency spectrum for different surfaces

Three surfaces surface 1, surface 2 and surface 3 were selected for the multiscale model. A stylus profilometer was used to measure the profiles of arbitrarily machined metal samples is shown in Figs. (5.2, 5.3, and 5.4). The displayed profile each comprised of 496 to 3900 data points. A frequency spectrum of the surface profile is also shown in Figs.(5.2, 5.3, and 5.4). The frequency spectrum (Fig. 5.2) of the surface 1 shows asperities of little

variation of amplitude with scale. The frequency spectrum plots for surface 2 and surface 3 show decreasing amplitudes with higher frequencies, as would normally be expected. Since the motivation behind this work was to develop a multiscale model incorporating the sinusoidal deformation model, the same material (Aluminum) with different levels of roughness was considered. The typical material properties that were defined were Young's modulus $E = 200GPa$, yield strength $S_y = 0.1GPa$, and Poisson's ratio $\nu = 0.33$. The sample length was 400μ .

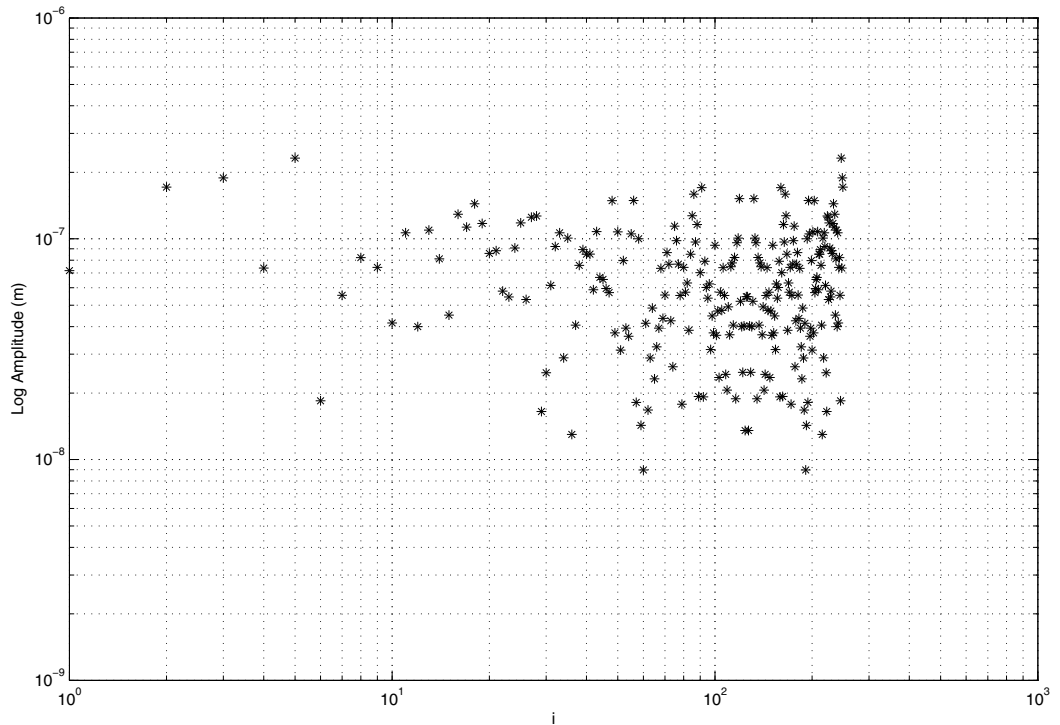


Figure 5.2: Frequency spectrum of surface 1.

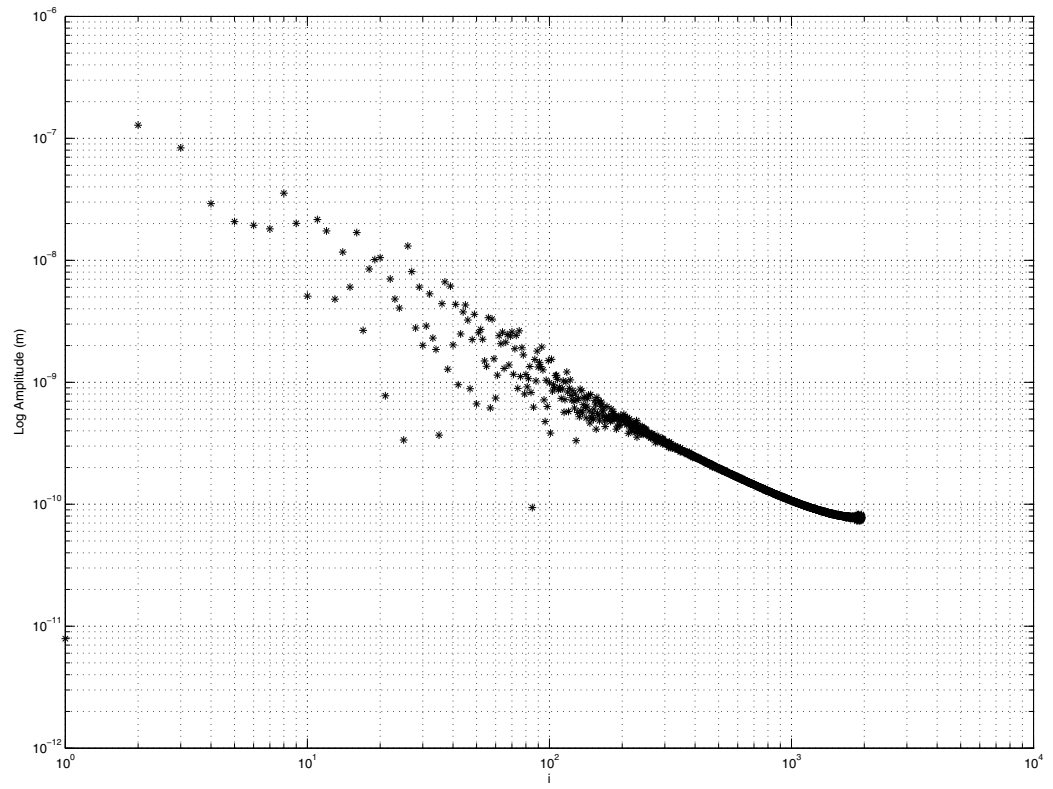


Figure 5.3: Frequency spectrum of surface 2.

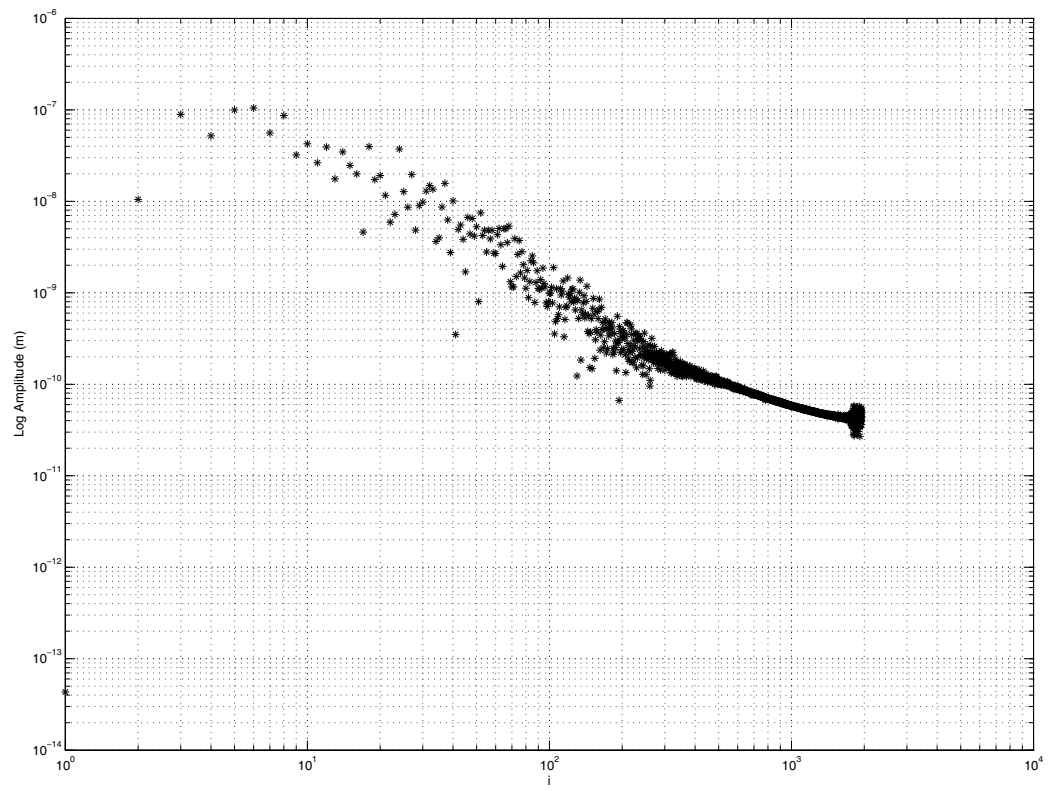


Figure 5.4: Frequency spectrum of surface 3.

5.5 Frequency level iteration versus contact area

To further emphasize how the multi-scale model works, the contact area as predicted by the model as a function of frequency level iteration, i , for two load cases $\frac{F}{A_n E'} = 9.774 \times 10^{-5}$ and $\frac{F}{A_n E'} = 9.774 \times 10^{-9}$ is shown in Figs. (5.5, 5.6, and 5.7). To see the trends from the elastic and the elasto-plastic multi-scale sinusoidal contact model, results from both the models are plotted alongside in the same figure. From Fig. (5.5) for the random surface sample, we can see that at higher loads the contact area for elasto-plastic case is close to 1 for the frequency range 10-100. The elastic case varies from .1 to 1 for the same load and frequency range. The drops in area occur due to the assumption 5 stated in the multiscale model foundation. For any given load level the contact area predicted by the immediate higher level cannot be more than the contact area predicted by the previous level. Based off of a visual inspection it is clear that both lower and higher frequency level ranges dictate the contact area prediction. This is a stark difference from the Jackson and Streater [14] model which considered surface 1 for the multiscale model. The contact area predicted by the Jackson and Streater model [14] is dictated by the lower frequency level ranges and the higher frequency level ranges have little to no effect on the contact area predicted. A possible reason for this difference could be the use of spherical asperity deformation model in their multiscale frame work. The surface profiles surfaces 2 and 3 that were considered in the multiscale model exhibit similar trends to the Jackson and Streater [14] multiscale model. This similarity is shown in Figs. (?? and ??) for these surface profiles.

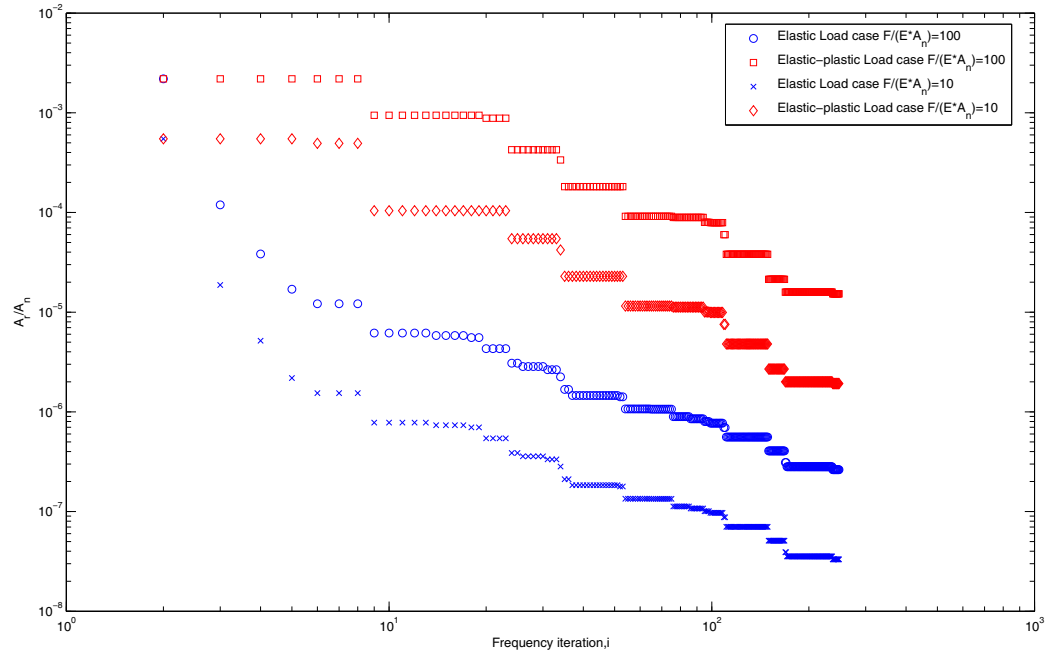


Figure 5.5: Contact area ratio versus frequency iteration for surface 1.

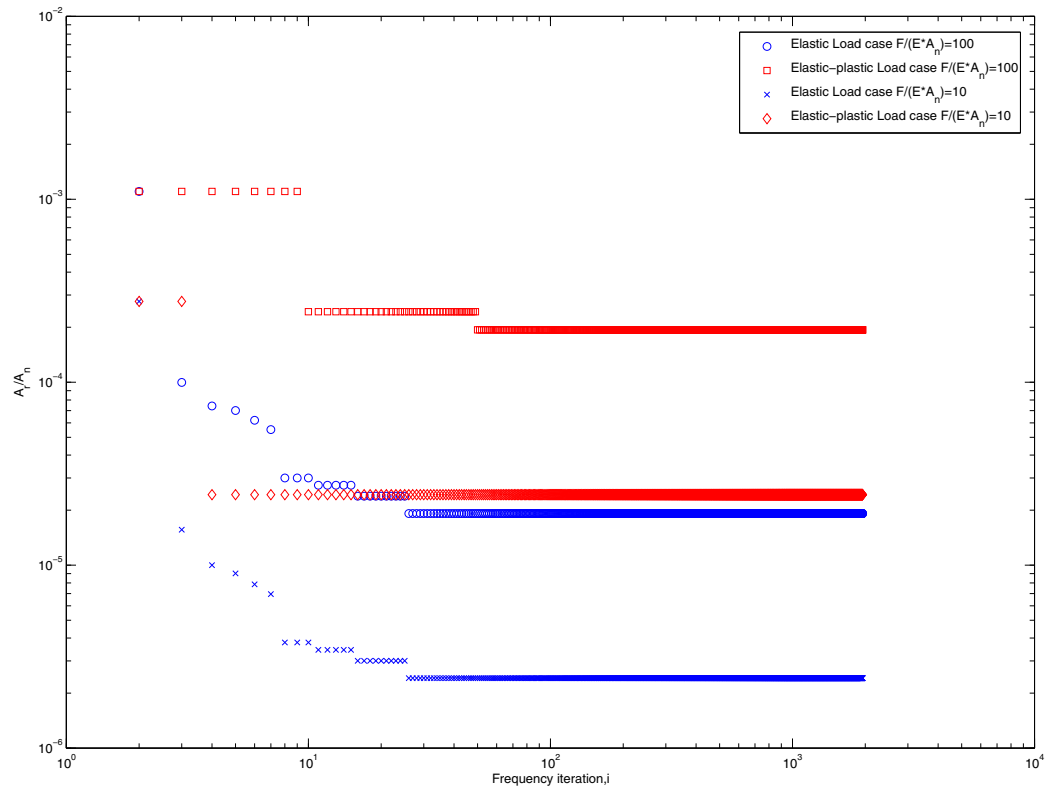


Figure 5.6: Contact area ratio versus frequency iteration for surface 2.

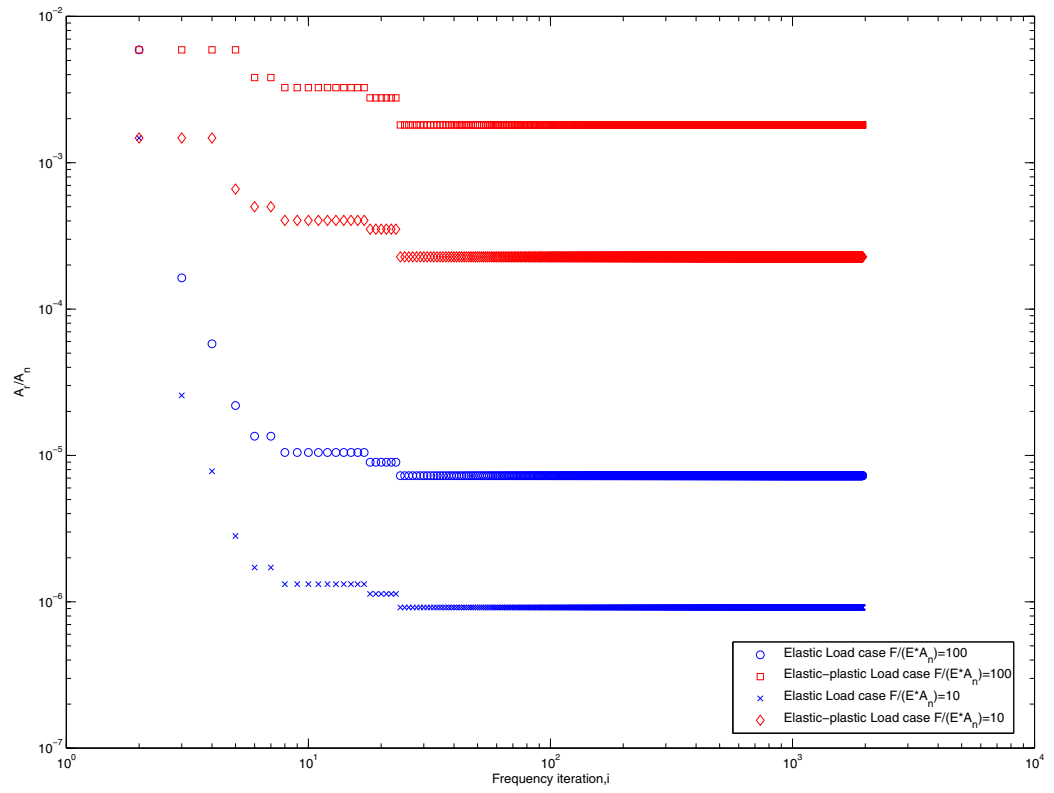


Figure 5.7: Contact area ratio versus frequency iteration for surface 3.

5.6 Elasto-plastic and elastic comparison

A comparison of elasto-plastic and elastic rough surface contact areas shows an expected trend. In Figs. (5.8, 5.9, and 5.9) we can see that model predicts a larger non-dimensional contact area as a function of non-dimensional surface load for the elasto-plastic case. This is in agreement with the fact that large contact areas are produced when a surface is deforming elasto-plastically. We can also see that the predicted real area of contact for both elastic and elasto- plastic as function of applied is linear in nature. The Greenwood et al. [29] statistical model and the Archard's [40] protuberence theory also show similar trends. Furthermore

Amonton's law of friction of can also be explained from the linear relationship between contact area and applied load. The real contact area predicted by the multiscale model is a function of the applied load. This relationship can be mathematically equated by introducing a non-dimensional contact factor.

$$A_r = C_s \cdot F_y \quad (5.7)$$

The friction force F_μ can be represented as a product of real area of contact and the Shear strength τ_y .

$$F_\mu = A_r \cdot \tau_y \quad (5.8)$$

Now, substituting for A_r from Eq. 5.7 into Eq. 5.8 yields the following:

$$F_\mu = C_s \cdot \tau_y \quad (5.9)$$

Eq. 5.9 can be viewed as the Amonton's law of friction for a body experiencing normal reaction on a rough surface. In other words, the friction force, F_{μ} , appears to be related to the normal force, F_y , by a constant friction coefficient. This is therefore in accordance with one of the empirical 'law of friction'. This model can also be used to predict electrical contact resistance and thermal contact resistance, adhesion and wear.

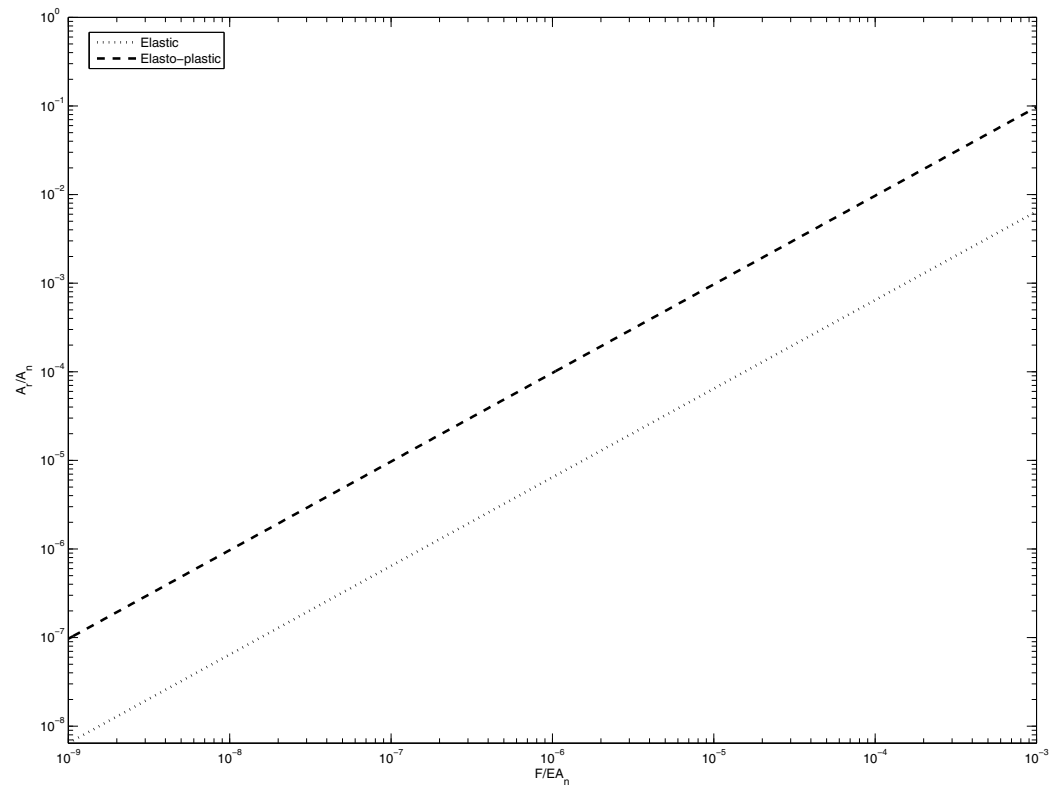


Figure 5.8: Elastic and Elasto-Plastic contact area versus applied load for surface 1.

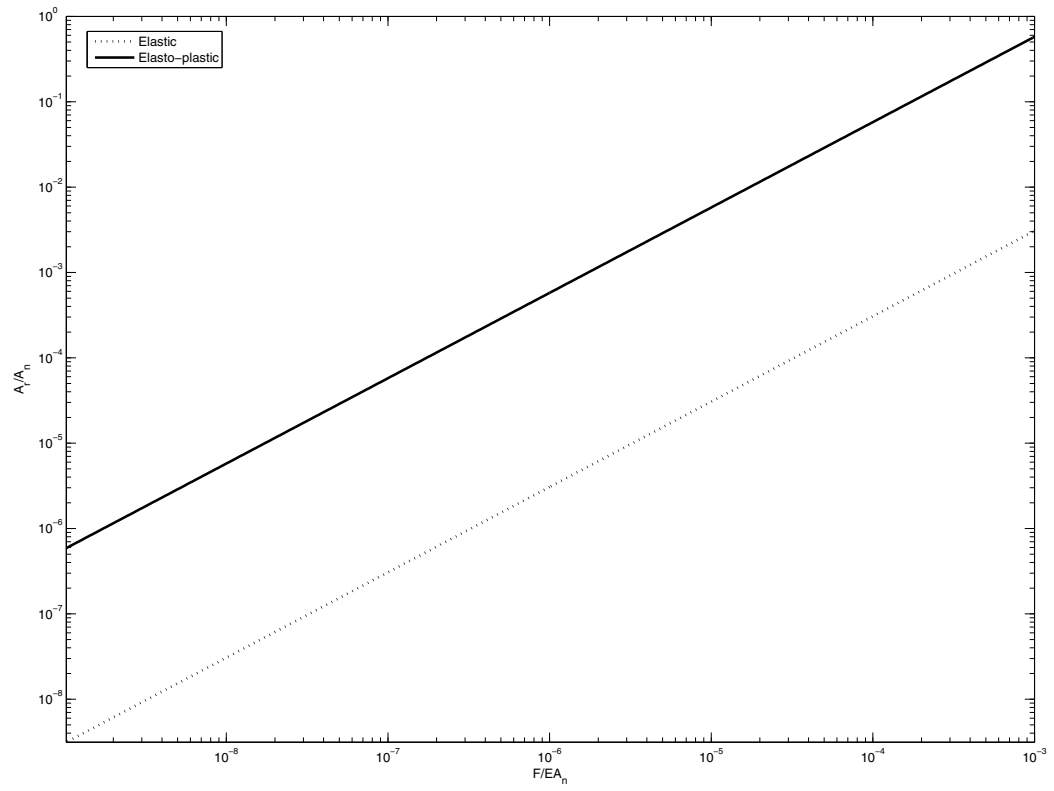


Figure 5.9: Elastic and Elasto-Plastic contact area versus applied load for surface 2.

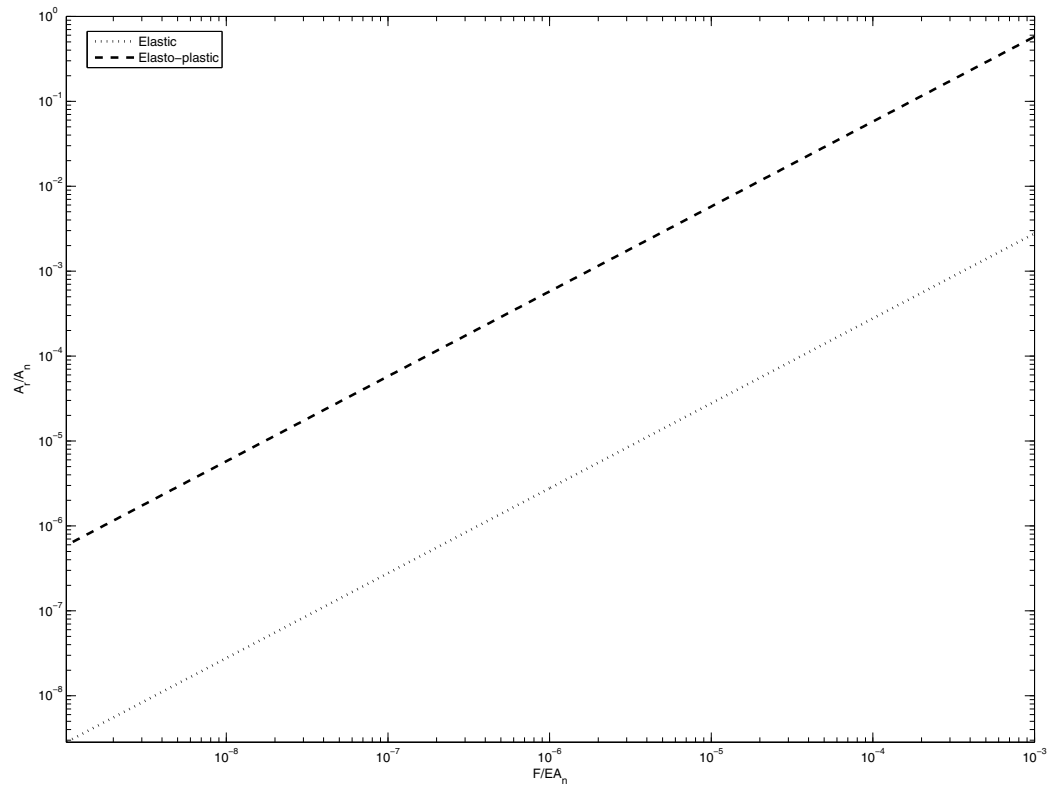


Figure 5.10: Elastic and Elasto-Plastic contact area versus applied load for surface 3.

CHAPTER 6

CONCLUSIONS

The contact problem comprised of an elasto-plastic deformable sinusoidal surface and a rigid flat was analyzed and modeled using the finite element method. The numerical analysis of the current finite element model provided an approximate solution for the elasto-plastic regime of sinusoidal contact. An empirical equation based on previous sinusoidal elastic contact models and elasto-plastic spherical contact models was formulated to fit the FEM data. Dimensionless expressions were empirically derived for the mean contact pressure which causes complete contact during large elasto-plastic deformations. By normalizing the contact area and the mean contact pressure, the current model provides analytical expressions of contact area as a function of pressure for the elasto-plastic regime. The expression for the contact area for the sinusoidal contact problem was obtained by modifying the Kogut and Etsion model [2] and the elastic sinusoidal models [1]. The errors in the numerical fits are fairly low (less than 5%) and suggest that the fits are reasonable. These equations should prove useful for modeling contact between rough periodically structured surfaces and in multiscale rough surface contact models.

The multiscale contact model utilizing the sinusoidal contact deformation model was developed for the elastic and the elasto-plastic cases. The contact area as a function of applied load was predicted using the model. The model predicted a linear trend as expected both for the elastic and the elasto-plastic sinusoidal asperity deformation models. The predicted area of contact was compared between the elastic and the elasto-plastic cases. As expected the elasto-plastic case predicted more area of contact. The frequency distribution

of surface profiles in a multiscale model is a Fourier series which is a series of sine and cosine wave forms. In keeping with inherent property of the model, the sinusoidal contact model seems to be a good choice for a asperity deformation model. The multi-scale model by Jackson and Streater [14] uses a spherical asperity deformation model for both elastic and elasto-plastic cases, which is different from the current multi-scale contact model. The most significant weakness of the multiscale model is the assumption that all asperities at a given frequency level exhibit deformation characteristics under identical load conditions. This means that a asperities of given wavelength may not reside at different heights.

BIBLIOGRAPHY

- [1] Johnson,K.L., Greenwood,J.A, and Higginson, J.G., *The contact of elastic regular wavy surfaces.*, Int.J.Mech.Sci., 1985. **27**(6): p. 383-396.
- [2] Kogut,L., and Etsion,I., *Elastic-plastic contact analysis of a sphere and a rigid flat.*, J. of Applied Mechanics, Trans. ASME,2002. **69**(5): p. 657-662.
- [3] Johnson,K.L., *Contact mechanics.*, Cambridge University Press., 1985.
- [4] Dyson, A., *Approximate calculations of Hertzian compressive stresses and contact dimensions*, J. of Mech. Engg. Sci., 1965. **98**(7): p. 214-224.
- [5] Galin, L.A., *Contact problems in the theory of elasticity*, Moscow., 1963.
- [6] Garg, V.K., Anand, S.C., and Hodge, P.G., *Elastic-plastic analysis of a wheel rolling on a rigid track*, Int.J.Solids and Structures, 1974. **10**(945): p. 290-295.
- [7] Goodman, L.E., *Contact stress analysis of normally loaded rough surfaces*, J. of Applied Mechanics, Trans. ASME,1962. **29**(515): p. 119-121.
- [8] Goodman, L.E., and Keer, L.M., *Elastic-plastic analysis of a wheel rolling on a rigid track*, Int.J.Solids and Structures, 1965. **1**(407): p. 110-117.
- [9] Johnson, K.L., *Surface interaction between elastically loaded bodies under tangential forces*, Proceedings, Royal Society, 1955. **A320**(531): p. 75-220.
- [10] Greenwood, J.A. and Tripp, J.H *The elastic contact of rough spheres*, J. of Applied Mechanics, Trans. ASME,1967. **34**(300): p. 417-420.
- [11] Westergaard,H.M., *Bearing pressure and cracks.*, ASME J. of Appl. Mech., 1939. **6**: p. 49-53.
- [12] Stanley,H.M. and Kato,T., *FFT-based method for rough surface contact.*, Journal of Tribology, Transactions of the ASME, 1997. **119**(3): p. 481-485.
- [13] Krithivasan.V., and Jackson,R.L., *An analysis of three-dimensional elasto-plastic sinusoidal contact.*, Trib.Letters., 2007. **27**(1): p. 31-43.
- [14] Jackson,R.L. and Streator,J.L., *A multiscale model for contact between rough surfaces.*, Wear, 2006. **261**(11-12): p. 1337-1347.

- [15] Bora,C.K, Flater,E.E, Street,M.D., Redmond,J.M., Starr,M.J., Carpick,R.W., and Plesha,M.E., *Multiscale roughness and modeling of MEMS interfaces.*, Tribology Letters, 2005. **19**(1): p. 37-48.
- [16] Ciavarella, M., Demelio, G., Barber, J.R., and Jang, Y.H., *Linear elastic contact of the weierstrass profile.*, Proc. R. Soc. Lond. A, 2000(456): p. 387-405.
- [17] Ciavarella, M., Murolo, G., Demelio, G., and Barber, J.R., *Elastic contact stiffness and contact resistance for the weierstrass profile.*, J. Mech. Phys. Solids, 2004. **52**(6): p. 1247-1265.
- [18] Gao, Y.F. and Bower, A.F., *Elastic-plastic contact of a rough surface with weierstrass profile.*, Proc. R. Soc. A, 2006. 462: p. 319-348.
- [19] Persson, B.N.J., *Elastoplastic contact between randomly rough surfaces.*, Physical Review Letters, 2001. **87**(11): p. 116101.
- [20] Persson, B.N.J., Bucher, F., and Chiaia, B., *Elastic contact between randomly rough surfaces: Comparison of theory with numerical results.*, Physical Review B, 2002. **65**: p. 184106-1.
- [21] Gao, Y.F., Bower, A.F., Kim, K.S., Lev, L., and Cheng, Y.T., *The behavior of an elastic-perfectly plastic sinusoidal surface under contact loading.*, Wear, 2006. **261**(2): p. 145-154.
- [22] Jackson, R.L. and Green, I., *A finite element study of elasto-plastic hemispherical contact.*, ASME J. Tribol., 2005. **127**(2): p. 343-354.
- [23] Quicksall, J.J., Jackson, R.L., and Green, I., *Elasto-plastic hemispherical contact models for various mechanical properties.*, IMechE J. of Eng. Trib. -Part J., 2004. **218**(4): p. 313-322.
- [24] Chaudhri, M.M., Hutchings, I. M., Makin, P. L., *Plastic compression of spheres.*, Philosophical Magazine, 1984. **49**(4): p. 493-503.
- [25] Greenwood, J.A. and Rowe, G.W., *Deformation of surface asperities during bulk plastic flow.*, J. Appl. Phys., 1965. **36**: p. 667-668.
- [26] Marsh, D.M., *Plastic flow in glass.*, Proc. R. Soc. A, 1964.**279**(6): p. 420-435.
- [27] Johnson, K.L., *The correlation of indentation experiments.*, J. Mech. Phys. Solids, 1970. **18**: p. 115-126.
- [28] Majumdar, A. and Bhushan, B., *Fractal model of elastic-plastic contact between rough surfaces.*, ASME J. of Tribol., 1991. **113**(1): p. 1-11.

- [29] Greenwood, J.A. and Williamson, J.B.P., *Contact of nominally flat surfaces.*, Proc. R. Soc. Lond., 1966. **A(295)**: p. 300-319.
- [30] Majumdar, A., and Tien, C. L., *Fractal characterization and simulation of rough surfaces*, Wear, 1990. **136**: p. 313-327.
- [31] Kogut, L., and Jackson, R. L., *A comparison of contact modeling utilizing statistical and fractal approaches*, ASME J. Tribol., 2006. **128**: p. 213-217.
- [32] McCool, J. I., *Comparison of models for the contact of rough surfaces*, Wear, 1986. **107**: p. 37-60.
- [33] Chang, W.R., Etsion, I., and Bogy, D. B., *An elastic-plastic model for the contact of rough surfaces*, ASME J. Tribol., 1987. **109(2)**: p. 257-263.
- [34] Yan, W., and Komvopoulos, K., *Contact analysis of elastic-plastic fractal surfaces*, J. Appl. Phys., 1988. **84**: p. 3617-3624.
- [35] Polycarpou, A., and Etsion, I., *Analytical approximations in modeling contact rough surfaces*, ASME J. Tribol., 1999. **121(2)**: p. 234-239.
- [36] Majumdar, A. and Bhushan, B., *Role of fractal geometry in roughness characterization and contact mechanics.*, ASME J. of Tribol., 1990. **112(2)**: p. 205-216.
- [37] Brizmer, V., Zait, Y., Kligerman, Y., and Etsion, I., *The effect of contact conditions and material properties on Elastic-Plastic Spherical Contact.*, J. Mech. Mater. Struct., 2006. **1(5)**: p. 865-879.
- [38] Kogut, L., and Etsion, I., *A finite element based elastic-plastic model for the contact of rough surfaces*, Tribol. Trans., 2003. **46**: p. 383-390.
- [39] Eid, H. and Adams, G. G., *An elastic-plastic finite element analysis of interacting asperities in contact with a rigid flat*, J. Appl. Phys., 2007. **40**: p. 7432-7439.
- [40] Archard, J.F., *Elastic deformation and the Laws of friction.*, Proc. R. Soc. Lond., 1957. **A(243)**: p. 190-205.

APPENDICES

APPENDIX A

DERIVATION OF CRITICAL VALUES FOR SINUSOIDAL CONTACT

The critical or initial interference to cause yielding can be derived independently of hardness as

$$\omega_c = \left(\frac{\pi \cdot C \cdot S_y^2}{2 \cdot E'} R \right) \quad (\text{A.1})$$

where C is given by

$$C = 1.295 \exp(0.736 \cdot \nu) \quad (\text{A.2})$$

and the Poisson's ratio of the material that has the lowest value of $C \cdot S_y$, and thus yields first should be used. The critical force, F_c is then calculated at the critical interference, ω_c , to be

$$F_c = \frac{4}{3} \left(\frac{R}{E'} \right)^2 \left(\frac{C}{2} \cdot \pi \cdot S_y \right)^3 \quad (\text{A.3})$$

Similarly, the critical contact area is

$$A_c = \pi^3 \left(\frac{C S_y R}{2 E'} \right)^2 \quad (\text{A.4})$$

By dividing the critical force (Eq. (A3)) by the critical area (Eq. (A4)) the critical contact pressure is defined as

$$p_c = \left(\frac{2CS_y}{3} \right) \quad (\text{A.5})$$

These critical values can be modified for use in the sinusoidal case considered in this work by substituting in the relation

$$R = \left(\frac{1}{4\pi^2\Delta f^2} \right) \quad (\text{A.6})$$

which is the radius of curvature for the tip of a sinusoidal surface. In addition, there are actually two sphere-like peaks of contact which occur during a λ^2 area of sinusoidal contact (see Fig. 1). This results in a modified critical force given by

$$F_c = \frac{1}{6\pi} \left(\frac{1}{\Delta f^2 E'} \right)^2 \left(\frac{C \cdot S_y}{2} \right)^3 \quad (\text{A.7})$$

Similarly, the modified critical contact area is

$$A_c = \frac{2}{\pi} \left(\frac{C \cdot S_y}{8\Delta f^2 E'} \right)^3 \quad (\text{A.8})$$

Since R does not appear in Eq. (A5), the critical pressure is not influenced by δ . It should be noted that Eqs. (A5, A7 and A8) are only valid for the initial stages of contact between sinusoidal surfaces (when the contacting surfaces are geometrically similar to

spheres). However, these critical values are useful in determining when a sinusoidal contact begins deforming in the elasto-plastic range.

APPENDIX B

MATLAB CODE FOR CONTACT AREA VERSUS FREQUENCY ITERATION

```
    hx = xlsread('sdata',1,'c2 : c3901');
    hx = hx * 10-10;
    v = length(hx);

    /*****Length of sample*****/

    L = 400e - 6;

    /*****Fourier transform of surface profile*****/

    v = v/2;
    Y = fft(hx,v)/v;
    v = v/2;
    YY = abs(Y);
    YY = sqrt(Y.*conj(Y));

    /*****Material properties*****/

    E = 1/(1 - .332) * 200 * 109;
    Sy = 1e8;
    v1 = 0.33;

    /*****Johnson area coefficients*****/

    w2 = 3/2/pi;
    w3 = sqrt(2) * pi * E;
    w4 = 3/8/pi;
    k = 1;

    /*****Initial area and Intial load*****/

    Ari = 3.3 * 1.5 * 10(-6);
    Fa = 0.0001 * E * Ari;

    /*****Highest level of applied load*****/
```

```

for(j = 100)
Lo = Fa * (10(j - 1)/100 - 5);
Lo1(j) = Lo/E/Ari;
Atotal(1) = Ari;
Atotal(2) = Atotal(1);
Atotalep(1) = Ari;
Atotalep(2) = Atotalep(1);

/*****Frequency level iteration*****/

for(i = 2 : v)

I(i - 1) = i;

/*****Amplitude and Frequency calculation*****/

beta = YY(i);
f = (i - 1)/L;
l = 1/f;
h = 2 * f2;
C3 = Lo/((Atotal(i - 1)));
pbar = (w3 * beta * f);
prat = C3/pbar;

/*****Elastic multiscale model*****/

if(C3 > pbar)
Af(i) = Atotal(i - 1)/h/Atotal(i - 1);
else

AJ1 = (2 * pi/f2) * (w4 * prat)(2/3);
AJ2 = (1/f2) * (1 - (w2) * (1 - prat));

/*****Area comparison for every frequency level*****/

if(prat < 0.8)

Af(i) = AJ1 * (1 - (prat)(1.51)) + AJ2 * (prat)(1.04);

else

Af(i) = AJ2;

```

```

end

end

Atotal(i) = Atotal(i - 1) * h * Af(i);

if(Atotal(i - 1) > Atotal(i))

a(j) = Atotal(i);
be(i - 1) = a(j)/Ari;

else

Atotal(i) = Atotal(i - 1);
a(j) = Atotal(i);
be(i - 1) = a(j)/Ari;

end

/*****Elasto-plastic multiscale model*****/

C4 = Lo/Atotalep(i - 1);
Fasp = C4/f2;
pbar = (w3 * beta * f);
pbarep = pbar * (4.172 * Sy/E + 0.0173) * sqrt(beta * f);

if(pbarep > pbar)
pbarep = pbar;
end

/*****Calculation of constants*****/

C = 1.295 * exp(0.736 * v1);
d = 3.8 * (E * beta/Sy/l)0.11;

/*****Critical area and Critical force*****/

Fcrit = 1/6/pi * (1/beta/f2/E)2 * (C/2 * Sy)3;
Acrit = (2/pi) * (C * Sy/8/beta/f2/E)2;

/*****Elasto-plastic area comparison*****/

```

```

if(Fasp > Fcrit)

if(C4 > pbarep)
Afep(i) = Atotalep(i - 1)/h/Atotalep(i - 1);
else

Aep = 2 * Acrit(d/(1 + d)) * (3 * C4/f2/4/C/Sy)(d/(1 + d));
AJ2ep = (1/f2) * (1 - 3/2/pi * (1 - C4/pbarep));
Afep(i) = Aep * (1 - (C4/pbarep)1.51) + AJ2ep * (C4/pbarep)1.04;

end

else

if(C4 > pbar)
Afep(i) = Atotalep(i - 1)/h/Atotalep(i - 1);
else

A1ep = (2 * pi/f2) * (3/8/pi * (C4/pbar))(2/3);
A2ep = (1/f2) * (1 - 3/2/pi * (1 - (C4/pbar)));
if((C4/pbar) < .8)
Afep(i) = A1ep * (1 - (C4/pbar)1.51) + A2ep * (C4/pbar)1.04;
else

Afep(i) = A2ep;

end

end

end

Atotalep(i) = Atotalep(i - 1) * h * Afep(i);

if(Atotalep(i - 1) > Atotalep(i))
bep(i - 1) = Atotalep(i);
b1ep(i - 1) = bep(i - 1)/Ari;
else

Atotalep(i) = Atotalep(i - 1);
bep(i - 1) = Atotalep(i);

```

```

blep(i - 1) = bep(i - 1)/Ari;
end

end

end

/*****Lowest level of applied load*****/

for(j = 10)
Lo = Fa * (10^(j - 1)/100 - 5);
Lo1(j) = Lo/E/Ari;
Atotal(1) = Ari;
Atotal(2) = Atotal(1);
Atotalep(1) = Ari;
Atotalep(2) = Atotalep(1);

/*****Frequency level iteration*****/

for(i = 2 : v)

I(i - 1) = i;

/*****Amplitude and Frequency calculation*****/

beta = YY(i);
f = (i - 1)/L;
l = 1/f;
h = 2 * f^2;
C3 = Lo/((Atotal(i - 1)));
pbar = (w3 * beta * f);
prat = C3/pbar;

/*****Elastic multiscale model*****/

if(C3 > pbar)
Af(i) = Atotal(i - 1)/h/Atotal(i - 1);
else

AJ1 = (2 * pi/f^2) * (w4 * prat)^(2/3);
AJ2 = (1/f^2) * (1 - (w2) * (1 - prat));

```



```

/*****Area comparison for every frequency level*****/

if(prat < 0.8)

Af(i) = AJ1 * (1 - (prat)(1.51)) + AJ2 * (prat)(1.04);

else

Af(i) = AJ2;

end

end

Atotal(i) = Atotal(i - 1) * h * Af(i);

if(Atotal(i - 1) > Atotal(i))

a(j) = Atotal(i);
be(i - 1) = a(j)/Ari;

else

Atotal(i) = Atotal(i - 1);
a(j) = Atotal(i);
be(i - 1) = a(j)/Ari;

end

/*****Elasto-plastic multiscale model*****/

C4 = Lo/Atotalep(i - 1);
Fasp = C4/f2;
pbar = (w3 * beta * f);
pbarep = pbar * (4.172 * Sy/E + 0.0173) * sqrt(beta * f);

if(pbarep > pbar)
pbarep = pbar;
end

/*****Calculation of constants*****/

```

```

C = 1.295 * exp(0.736 * v1);
d = 3.8 * (E * beta/Sy/l)0.11;

/*****Critical area and Critical force*****/

Fcrit = 1/6/pi * (1/beta/f2/E)2 * (C/2 * Sy)3;
Acrit = (2/pi) * (C * Sy/8/beta/f2/E)2;

/*****Elasto-plastic area comparison*****/

if(Fasp > Fcrit)

if(C4 > pbarep)
Afep(i) = Atotalep(i - 1)/h/Atotalep(i - 1);
else

Aep = 2 * Acrit(d/(1 + d)) * (3 * C4/f2/4/C/Sy)(d/(1 + d));
AJ2ep = (1/f2) * (1 - 3/2/pi * (1 - C4/pbarep));
Afep(i) = Aep * (1 - (C4/pbarep)1.51) + AJ2ep * (C4/pbarep)1.04;

end

else

if(C4 > pbar)
Afep(i) = Atotalep(i - 1)/h/Atotalep(i - 1);
else

A1ep = (2 * pi/f2) * (3/8/pi * (C4/pbar))(2/3);
A2ep = (1/f2) * (1 - 3/2/pi * (1 - (C4/pbar)));
if((C4/pbar) < .8)
Afep(i) = A1ep * (1 - (C4/pbar)1.51) + A2ep * (C4/pbar)1.04;
else

Afep(i) = A2ep;

end

end

end

```

```

Atotalep(i) = Atotalep(i - 1) * h * Afep(i);

if(Atotalep(i - 1) > Atotalep(i))
bep(i - 1) = Atotalep(i);
b1ep(i - 1) = bep(i - 1)/Ari;
else

Atotalep(i) = Atotalep(i - 1);
bep(i - 1) = Atotalep(i);
b1ep(i - 1) = bep(i - 1)/Ari;
end

end

end

figure(1);
loglog(I, be, 'bo', I, b1ep, 'rs', I, b2e, 'bx', I, b21ep, 'rd')
xlabel('Frequencyiteration, i')
ylabel('Ar/A_n')
set(z, 'Interpreter', 'tex')

```

APPENDIX C

MATLAB CODE FOR FREQUENCY SPECTRUM AND LOAD VERSUS

CONTACT AREA

```
    hx = xlsread('sdata', 1, 'b2 : b3901');
    hx = hx * 10-10;

    /*****Length of the sample*****/

    v = length(hx);
    L = 400e - 6;

    /*****Fourier transform of surface profile*****/

    v = v/2;
    Y = fft(hx, v)/v;
    v = v/2;
    YY = sqrt(Y .* conj(Y));

    /*****Material properties*****/

    E = 1/(1 - .332) * 200e9;
    Sy = 1e9;
    v1 = 0.33;

    /*****Johnson area coefficients*****/

    w2 = 3/2/pi;
    w3 = sqrt(2) * pi * E;
    w4 = 3/8/pi;
    k = 1;

    /*****Nominal area and Initial Load*****/

    Ari = 3.3 * 1.5 * 10(- 6);
    Fa = 0.0001 * E * Ari;

    I = 1 : 1 : v + 1;
```

```

II = log(I);

/*****Load iteration procedure from the initial load*****/

for(j = 1 : 1 : 1000)
Lo = Fa * (105 - (j - 1)/100);
Lo1(j) = Lo/E/Ari;
Atotal(1) = Ari;
Atotal(2) = Atotal(1);
Atotalep(1) = Ari;
Atotalep(2) = Atotalep(1);

/*****Frequency iteration for every level of applied load*****/

for(i = 2 : v)

/*****Amplitude and Frequency calculation*****/

beta = YY(i);
f = (i - 1)/L;
l = 1/f;
h = 2 * f2;
C3 = Lo/((Atotal(i - 1)));

/*****Elastic multiscale model*****/

/*****Critical pressure and pressure ratio for elastic case*****/

pbar = (w3 * beta * f);
prat = C3/pbar;

/*****Area comparison for every frequency level*****/

if(C3 > pbar)
Af(i) = Atotal(i - 1)/h/Atotal(i - 1);
else
AJ1 = (2 * pi/f2) * (w4 * prat)(2/3);
AJ2 = (1/f2) * (1 - (w2) * (1 - prat));

if(prat < 0.8)
if(i) = AJ1 * (1 - (prat)(1.51)) + AJ2 * (prat)(1.04);
else

```

```

Af(i) = AJ2;
end
end
Atotal(i) = Atotal(i - 1) * h * Af(i);

if(Atotal(i - 1) > Atotal(i))
a(j) = Atotal(i);
else
Atotal(i) = Atotal(i - 1); v
a(j) = Atotal(i);

end

/*****Elasto-plastic multiscale model*****/

/*****Initial load, asperity force and critical pressure calculation*****/

C4 = Lo/Atotalep(i - 1);
Fasp = C4/f2;
pbar = (w3 * beta * f);
pbarep = pbar * (4.172 * Sy/E + 0.0173) * sqrt(l/beta);

/*****Comparing elastic and elasto-plastic critical pressures*****/

if(pbarep > pbar)
pbarep = pbar;
end

/*****Calculation of constants for elasto-plastic case*****/

C = 1.295 * exp(0.736 * v1);
d = 3.8 * (E * beta/Sy/l)0.11;
Fcrit = 1/6/pi * (1/beta/f2/E)2 * (C/2 * Sy)3;
Acrit = (2/pi) * (C * Sy/8/beta/f2/E)2;

/*****Comparing asperity and critical force*****/

if(Fasp > Fcrit)
if(C4 > pbarep)
Afeep(i) = Atotalep(i - 1)/h/Atotalep(i - 1);
else

```

```

/*****Elasto-plastic area comparison*****/

Aep = 2 * Acrit(1/(1 + d)) * (3 * C4/f2/4/C/Sy)d/(1 + d);
AJ2ep = (1/f2) * (1 - 3/2/pi * (1 - C4/pbarep));
Afep(i) = Aep * (1 - (C4/pbarep)1.51) + AJ2ep * (C4/pbarep)1.04;
end
else
if(C4 > pbar)

Afep(i) = Atotalep(i - 1)/h/Atotalep(i - 1);
else

A1ep = (2 * pi/f2) * (3/8/pi * (C4/pbar))2/3;
A2ep = (1/f2) * (1 - 3/2/pi * (1 - (C4/pbar)));
if((C4/pbar) < .8)
Afep(i) = A1ep * (1 - (C4/pbar)1.51) + A2ep * (C4/pbar)1.04;
else
Afep(i) = A2ep;
end
end
end

Atotalep(i) = Atotalep(i - 1) * h * Afep(i);
if(Atotalep(i - 1) > Atotalep(i))
b(j) = Atotalep(i);
else
Atotalep(i) = Atotalep(i - 1);
b(j) = Atotalep(i);

end

end

aar(j) = a(j)/Ari;
aarep(j) = b(j)/Ari;
end

xlswrite('ssdata', aar', 1, d1')
xlswrite('ssdata', aarep', 1, e1')

```

```

/*****Plots*****/

figure(2);
loglog(Lo1, aar, 'k : ', Lo1, aarep, 'k - x')
axis([010e - 4010e - 1])
xlabel('F/EA_n')
ylabel('A_r/A_n')
z = legend('Elastic', 'Elasto - plastic', 2);
set(z, 'Interpreter', 'tex')

figure(3);
x = logspace(-1, 3);
loglog(I, YY(1 : v + 1), 'k*')
xlabel('i')
ylabel('LogAmplitude(m)')
gridon

```